MIRELLA: a mathematical model explains the effect of microRNA-mediated synthetic genes regulation on intracellular resource allocation

3452–3464 *Nucleic Acids Research, 2023, Vol. 51, No. 7* *Published online 13 March 2023*
https://doi.org/10.1093/nar/gkad151

MIRELLA: a mathematical model explains the effect of microRNA-mediated synthetic genes regulation on intracellular resource allocation

Federica Cella[1,7,†], Giansimone Perrino[3,†], Fabiana Tedeschi[1,2], Gabriella Viero[4], Carla Bosia[5,6], Guy-Bart Stan[3,*] and Velia Siciliano[1,*]

[1]Istituto Italiano di Tecnologia-IIT, Largo Barsanti e Matteucci, Naples, Italy, [2]University of Naples Federico II, Naples, Italy, [3]Department of Bioengineering and Centre of Excellence in Synthetic Biology, Imperial College London, London, UK, [4]Institute of Biophysics, CNR Trento, Povo, Italy, [5]Department of Applied Science and Technology, Politecnico di Torino, Torino, Italy, [6]Italian Institute for Genomic Medicine, c/o IRCCS, Candiolo, Italy and [7]Present address: Department of Biosystems Science and Engineering (D-BSSE), ETH Zürich, Mattenstrasse 26, Basel 4058, Switzerland

Received October 28, 2022; Revised January 11, 2023; Editorial Decision February 14, 2023; Accepted February 21, 2023

ABSTRACT

Competition for intracellular resources, also known as gene expression burden, induces coupling between independently co-expressed genes, a detrimental effect on predictability and reliability of gene circuits in mammalian cells. We recently showed that microRNA (miRNA)-mediated target downregulation correlates with the upregulation of a co-expressed gene, and by exploiting miRNAs-based incoherent-feed-forward loops (iFFLs) we stabilise a gene of interest against burden. Considering these findings, we speculate that miRNA-mediated gene downregulation causes cellular resource redistribution. Despite the extensive use of miRNA in synthetic circuits regulation, this indirect effect was never reported before. Here we developed a synthetic genetic system that embeds miRNA regulation, and a mathematical model, MIRELLA, to unravel the miRNA (MI) RoIE on intracellular resource aLLocAtion. We report that the link between miRNA-gene downregulation and independent genes upregulation is a result of the concerted action of ribosome redistribution and 'queueing-effect' on the RNA degradation pathway. Taken together, our results provide for the first time insights into the hidden regulatory interaction of miRNA-based synthetic networks, potentially relevant also in endogenous gene regulation. Our observations allow to define rules for complexity- and context-aware design of genetic circuits, in which transgenes co-expression can be modulated by tuning resource availability via number and location of miRNA target sites.

GRAPHICAL ABSTRACT

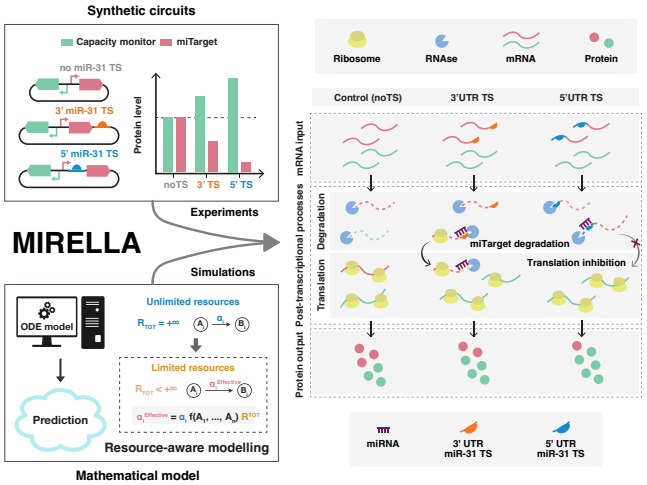

INTRODUCTION

Engineering mammalian cells with synthetic regulatory networks to obtain novel functionalities with predictable behaviour, requires a deep understanding of the dynamic interactions between the genetic circuits and the intracellular context in which they are intended to operate.

We recently showed that when exogenous DNAs are transiently delivered to mammalian cells, they compete for

*To whom correspondence should be addressed. Tel: +44 207 59 46375; Email: g.stan@imperial.ac.uk
Correspondence may also be addressed to Velia Siciliano. Tel: +39 08119933121; Email: velia.siciliano@iit.it
†The authors wish it to be known that, in their opinion, the first two authors should be regarded as Joint First Authors.

limited shared transcriptional and translational resources, reshaping RNA and protein levels, and leading to the coupling of otherwise independent genes (1,2). This becomes a pervasive problem, either when implementing regulatory circuits, or in attempts to carry out studies using system perturbations (i.e. overexpression or downregulation of a transient gene). The observation that synthetic circuits impose a gene expression burden to their host cells (1,3,4), prompted the development of '*context-aware*' gene networks in which incoherent feedforward loops (iFFLs) that use biomolecular controllers such as endoribonucleases (2), or endogenous and synthetic miRNAs (1) were successfully exploited as burden mitigators. In miRNA-based iFFL, we observed that the protein levels of two independently expressed genes, one of which was regulated by miRNA, were strongly linked to the miRNA activity (1). As a point in case, using two co-expressed fluorescent proteins, EGFP and mKate, with mKate levels linked by design to the endogenous miRNA-31 (miR-31), we showed that the higher the number of miRNA target sites (TS) in the mKate UTRs, the stronger its downregulation, and the higher the levels of EGFP (Figure 1A). Conversely, by inhibiting miR-31, mKate levels increased, counterbalanced by reduced EGFP levels (1), supporting the miRNA-dependency of the observed effect. Results were robust to changing plasmid design (co-transfection *vs* single plasmid) and cellular context (1).

Given the biological importance and high applicability of miRNAs to synthetic circuits, we sought to investigate the molecular mechanisms involved in miRNA-dependent resource distribution. We postulate that this understanding will enable more precise circuits' design with enhanced robustness and predictability, and may shed light on the secondary regulatory effect in endogenous pathways.

miRNAs are small non-coding RNAs produced from transcripts with stem-loop structures which undergo processing both in the nucleus and cytoplasm to be converted into mature, 21–26 nucleotides-long miRNAs. Mature miRNAs are assembled into the RNA-induced silencing complex (RISC) and bind their target mRNAs by base pairing usually to their 3'UTR or 5'UTR (5,6). Upon binding, miRNAs modulate their target through mRNA degradation and/or translational repression (7,8). Target sites (TS) can be fully or partially complementary to the miRNA. In the former case, the target is degraded through endonucleolytic cleavage (9), while in the latter translational repression dominates and transcript degradation occurs after deadenylation (7,8). Typically, in mammalian cells miRNAs bind to the 3'UTR of the endogenous target mRNA, and have non-perfect complementarity to the TS (7). Thus, their main mechanism of action is to repress translation. Moreover, miRNAs are often found in endogenous feedforward or negative feedback loops exploiting additional functions such as buffering gene expression against noise or fluctuations in external inducer concentration (10–13).

In synthetic biology, miRNAs have been repurposed as a versatile tool to build cell-specific devices, and have been largely used to create cell classifiers with biotechnological or biomedical applications (14,15) or to modulate the expression of the genetic devices (16,17). In these applications, to achieve strong downmodulation of the target genes, and increase the sensitivity to small concentrations of miRNAs, perfectly complementary target sites are typically used (18).

Here, we use a two-gene reporter system (EGFP hereafter named *capacity monitor*, and miR31TS-mKate, hereafter named *miTarget*), along with a mathematical model (MIRELLA) that qualitatively captures post-transcriptional events, to explain the effect of miRNA (MI) REgulation on intracellular resource aLLocAtion, effectively identifying key processes responsible for miRNA-based burden mitigation in mammalian cells (Figure 1A, B).

MIRELLA builds on an existing modelling framework (1) and considers that mRNA translation and degradation use pools of shared resources, among which we account as main players ribosomes and RNases, respectively. MIRELLA replaces reaction rates that involve shared cellular resources with effective reaction rates that account for the availability of each individual resource pool according to the overall gene expression demand (Figure 1B). We use MIRELLA to predict the effect of miRNA regulation on resource availability considering the strength of the downregulation (number of target sites), and the effect of TS location (i.e. as part of the 5'UTR or 3'UTR). The model suggests that miRNA-mediated downregulation of the target mRNAs causes a redistribution of translational resources (i.e. ribosomes) and impacts the RNA degradation machinery, overall contributing to a change in protein expression levels (Figure 1C). We then experimentally validated the model predictions for the expression of exogenous and endogenous genes.

Supported by the synergistic use of a mathematical model and experiments, our findings contribute to a deeper understanding of the mechanisms of miRNA operations in synthetic networks, which enables the resource-aware design of genetic circuits. Moreover, our results provide insights into secondary effects of miRNA regulation that might be potentially relevant also in endogenous gene regulation.

MATERIALS AND METHODS

DNA cloning and plasmid construction

Plasmid vectors carrying gene cassettes were created using In-Fusion HD cloning kit (Clontech), or digestion and ligation. Reaction included 1:2 molar ratio of plasmid backbone:gene inserts starting with 100 ng of vector backbone digested with selected restriction enzymes. All plasmids used in this study consist of a constitutive promoter driving the gene of interest. All plasmids used in this study were confirmed by sequencing analysis and are listed in Supplementary Table 2.

Cell culture

H1299 cells were maintained in Roswell Park Memorial Institute medium (RPMI, Gibco) supplemented with 10% FBS (Atlanta BIO), 1% penicillin/streptomycin/L-glutamine (Sigma-Aldrich) and 1% non-essential amino acids (HyClone). The cells were maintained at 37°C and 5% CO_2.

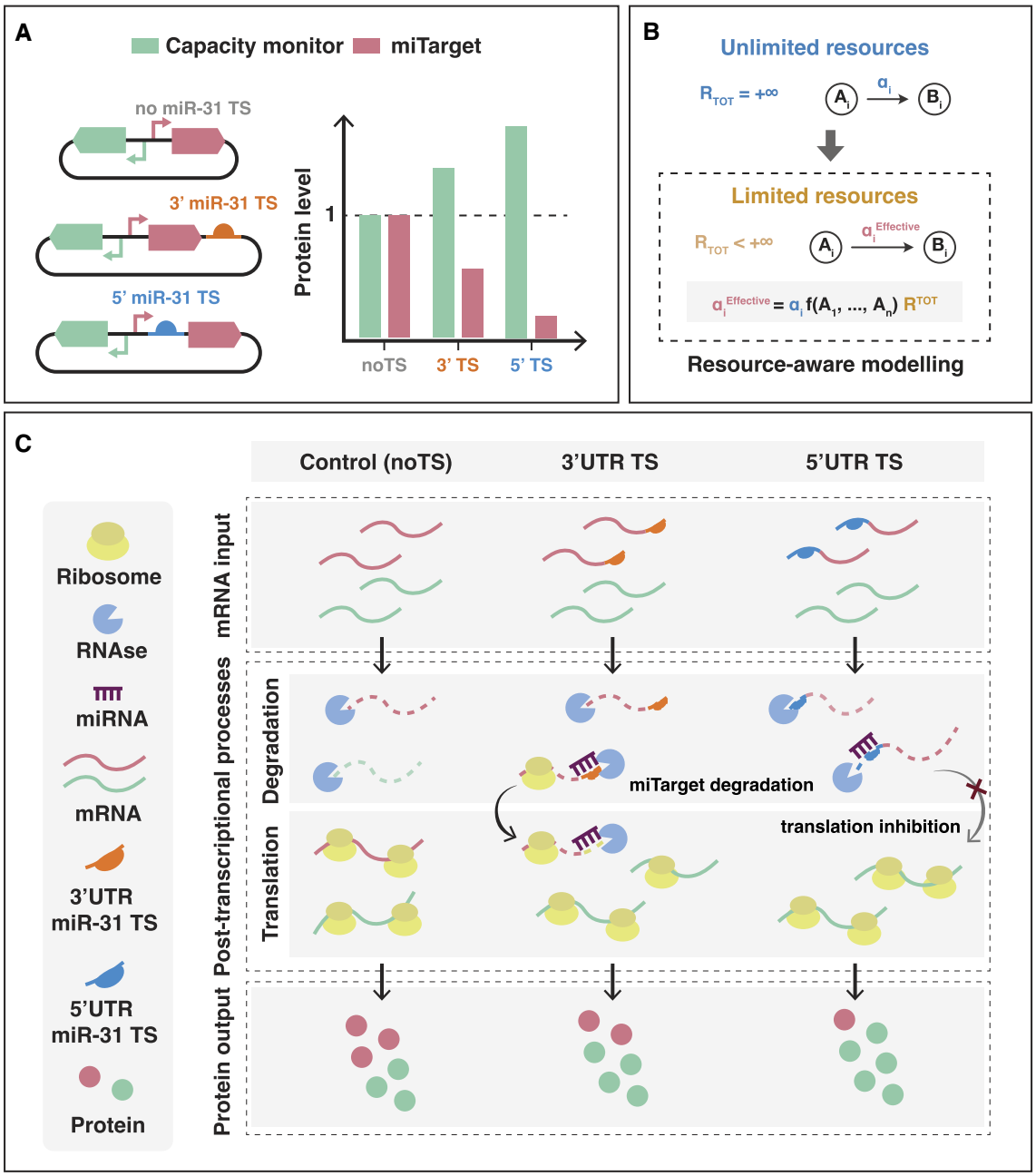

Figure 1. Graphical abstract of the study. (**A**) Graphical representation of the effect of the downregulation of a transgene (mKate-*miTarget*, red) by endogenous miRNAs (e.g. miR-31), on a co-expressed gene (*capacity monitor*, green) (1). The stronger the downregulation of the *miTarget*, the more the upregulation of the *capacity monitor*, in a miRNA target sites (TS) number- and location-fashion 5'UTR (blue) or 3'UTR (orange). (**B**) Modelling of gene networks in a resource-limited context. MIRELLA replaces all reaction rates (α_i) that involve shared cellular resources with their corresponding effective reaction rates (namely α_i^{Eff}) that capture the availability of that resources according to the overall demand from competing genes (modelled via the general function $f(\ldots)$). (**C**) Effect of miRNA activity on protein expression in a finite-resource context. Control (noTS): protein expression in the absence of miRNA regulation. TS in the 5' or 3'UTR: the slicer activity of miRNA-RISC complex triggers mRNA degradation of the *miTarget* (red) causing a queueing effect on the degradation of other mRNAs that results in *capacity monitor* (green) protein accumulation. TS in the 5'UTR: in addition to slicer activity, miRNA binding inhibits translation initiation, freeing up translational resources to the benefit of other transcripts (e.g. the *capacity monitor*). The resulting effect is stronger downregulation of *miTarget* and higher *capacity monitor* levels when TS are placed in the 5'UTR of the *miTarget*.

Transfection

Transfections were carried out in 24-well plate format for flow cytometry analysis, in 12-well plate format for flow cytometry and qPCR analyses run on the same biological replicate or in 10 cm dishes for polysome profiling. H1299 cells were transfected with Lipofectamine® 3000 (Thermo Fisher Scientific) according to the manufacturer's instructions and 300 ng of total DNA for each sample for a transfection in 24-well plates and scaled up for larger formats. Details on transfections are provided in Supplementary Table 1.

Flow cytometry and data analysis

Cells were analysed using a BD FACSAria™ cell analyser (BD Biosciences) using 488 nm and 561 nm lasers. Cells transfected in 12-well plates were washed with DPBS, detached with 100 μl of trypsin–EDTA (0.25%) phenol red and resuspended in 600 μl of DPBS (Thermo Fisher Scientific). 200 μl of cell suspension were used for flow cytometry and 400 μl for RNA extraction. For each analysis, 10 000+ events from each sample were recorded and data were normalised with three compensation controls: unstained (wild-type cells), and single colour controls (mKate only, EGFP only). Fluorescence intensity in arbitrary units (AU) was used as a measure of protein expression. Population of live cells was selected according to FCS/SSC parameters. Data analysis was performed with Cytoflow. For each sample, we gated the population of live cells and then the $EGFP^+mKate^+$ cells (Q2 quadrant in Supplementary Figure 9b). Within this population we calculated the geometric mean (Geo-Mean) of mKate and EGFP.

Polysome profiling

Polysome profiling was performed following the protocols described in (19,20). To obtain the cytoplasmic lysates, cells were treated with cycloheximide (10 μg ml^{-1}) for 3–4 min and then lysed in 300 μl of cold hypotonic lysis buffer (19). To remove nuclei, mitochondria and cellular debris, the lysates were centrifuged at 4°C for 5 min at 20 000 g. To separate ribosomal subunits, ribosomes and polysomes from other cytoplasmic molecules, the supernatant was loaded on a 10–40% (w/v) sucrose gradient and centrifuged for 1 h 30 min at 260 000 g at 4°C in a SW41 rotor using a Beckman Optima LE-80 Ultracentrifuge. Twelve 1 ml fractions were collected and the absorbance at 254 nm was monitored with the UA-6 UV/VIS detector (Teledyne Isco). RNA was purified fraction by fraction using the phenol/chloroform extraction method described in (21). The retro-transcription reaction was performed using the same volume of RNA for all polysomal fractions. The co-sedimentation profile of mRNAs was obtained by calculating the percentage (or fraction) of mRNAs in each fraction by qPCR as described in (22).

mRNA half-life measurement upon DRB treatment

mRNA half-life was measured by treating H1299 cells 24 h post-transfection with 5,6-dichlorobenzimidazole 1-β-D-ribofuranoside–DRB (Sigma-Aldrich) 50 μM. Cells were collected at different time-points (0 h, 0 h 30 min, 1 h, 1 h 30 min, 2 h, 3 h, 4 h after treatment) for RNA extraction and qPCR analysis.

mRNA extraction and reverse transcription

RNA extraction was performed with E.Z.N.A.® Total RNA Kit I (Omega Bio-tek). Protocol was followed according to the manufacturer's instructions and RNA was eluted in 30 μl of RNase-free water to maximise the yield. RNA samples were conserved at –80°C. The protocol was performed exclusively with RNase free water in an RNase-free environment.

PrimeScript RT Reagent Kit with gDNA Eraser—Perfect Real Time (Takara) was used according to manufacturer's instructions. The protocol was performed on ice in a RNase-free environment to avoid RNA degradation. A negative control without PrimeScript RT Enzyme Mix I was always prepared to be sure that samples were not contaminated with genomic DNA.

qPCR

Fast SYBR Green Master Mix (Thermo Fisher Scientific) was used to perform qPCR of cDNAs obtained from 500 ng of RNA and diluted 1:5. Samples were loaded in MicroAmp™ Fast Optical 96-Well Reaction Plate (0.1 ml) and the experiment was carried out with a 7900HT™ Fast machine. Each well contained 10 μl of final volume (5 μl SYBR Green Master Mix 2X, 2 μl ddH2O, 1 μl of each primer, 1 μl of template). Also, a control without template (blank) was set. Primers were designed to amplify a region of 60–200 bp (Supplementary Table 3) and with a temperature of annealing between 50°C and 65°C. Data were analysed using the Comparative Ct Method according to Applied Biosystems Protocols.

Modelling

We constructed a deterministic ODE model to qualitatively capture post-transcriptional events in order to identify key processes responsible for miRNA-based resource reallocation. Our ODE model is based on a previously published resource-aware modelling framework (1). Full details of its formulation and parameterisation can be found in Supplementary Notes 1–6, Supplementary Tables 4–7, and Supplementary Figures 1–2, 6–7.

Deterministic simulations of the ODE model

All the simulations of the ODE model were run using Python 3 (v. 3.8.13). The *scipy.integrate.solve_ivp* function from the *SciPy* library (v. 1.8.0) was used to numerically integrate the ODE model. More specifically, we used the *Radau* method (stiff ODE solver) with an absolute tolerance of 10^{-9}, and a relative tolerance of 10^{-6}. To simulate the ODE model at steady state, the time span was set to [0, 10 000] h. Hence, steady state was taken as the value for each molecular species at the end of a numerical simulation of 10 000 h.

The parameter values used to simulate the ODE model were chosen as described in Supplementary Note 6 and reported in Supplementary Table 5 (for simulations of the translational resource reallocation) and Supplementary Table 7 (for simulations of the degradation resource reallocation). All plots were generated in Python using the *Matplotlib* library (v. 3.5.1). The code to run all the simulations and the model is available publicly as Jupyter notebooks (https://github.com/giansimone/MIRELLA/).

Analytical characterisation of the translational resource reallocation

To quantitatively characterise the reallocation of the translational resources at steady state, we derived an analytical solution of the ODE model as reported in Supplementary Note 1. Full details of the analytical solution derivation can be found in Supplementary Note 4. The steady-state expression levels for both the *miTarget* ($\bar{p}_T$) and the *capacity monitor* ($\bar{p}_C$) are as follows:

$$\bar{p}_T = \frac{\gamma_T}{\delta_T} \cdot \frac{\rho_T + \sigma\ \rho_T^Q}{1 + \rho_C + \rho_T + \sigma\ \rho_T^Q} \cdot r^{Total} \tag{1a}$$

$$\bar{p}_C = \frac{\gamma_C}{\delta_C} \cdot \frac{\rho_C}{1 + \rho_T + \sigma\ \rho_T^Q + \rho_C} \cdot r^{Total} \tag{1b}$$

where ρ_T is the resource demand coefficient for the *miTarget*, ρ_T^Q is the resource demand coefficient for the *miTarget:miRNA* complex, and ρ_C is the resource demand coefficient for the *capacity monitor*. The boolean parameter $\sigma \in \{0, 1\}$ captures the location of the miR-TS at either the 5' ($\sigma = 0$) or 3' ($\sigma = 1$) UTRs. The analytical expressions of the resource demand coefficients are as follows:

$$\rho_T = \frac{n_T\, \alpha_T}{\kappa_T \left(\beta_T + \frac{\alpha_Q\ \eta^+\ \beta_T^Q}{\beta_Q\ (\beta_T^Q + \eta^-)}\right)} \tag{2a}$$

$$\rho_T^Q = \frac{n_T\, \alpha_T}{\kappa_T \left(\beta_T^Q + \frac{\beta_T\ \beta_Q\ (\beta_T^Q + \eta^-)}{\alpha_Q\ \eta^+}\right)} \tag{2b}$$

$$\rho_C = \frac{n_C\, \alpha_C}{\kappa_C\, \beta_C} \tag{2c}$$

where κ_T and κ_C are the effective dissociation constant for the *miTarget* and *capacity monitor*, respectively (see Supplementary Note 1 for their definitions). All other parameters are described in Supplementary Table 5.

Model fitting

The model fitting shown in Supplementary Figure 3 was performed using Python 3 (v. 3.8.13). The *scipy.optimize.differential_evolution* function from the *SciPy library* (v. 1.8.0) was used to find the model parameters that best fit the predicted steady-state expression levels for both the *miTarget* and *capacity monitor* to the experimental data reported in Figure 2B. The error distance between the predicted and the experimental data was evaluated using the following loss function:

$$L(\vartheta) = ||y - \hat{y}\ ||_2^2 + \lambda\ ||\ \vartheta\ ||_2^2$$

where $y = [y_{Control},\ y_{1TS\,3'},\ y_{1TS\,5'},\ y_{3TS\,3'},\ y_{3TS\,5'}]^T$ is the vector that contains the different mean values for the *miTarget* (mKate) and the *capacity monitor* (EGFP) in each condition as reported in Figure 2b, $\hat{y} = [\hat{y}_{Control},\ \hat{y}_{1TS\,3'},\ \hat{y}_{1TS\,5'},\ \hat{y}_{3TS\,3'},\ \hat{y}_{3TS\,5'}]^T$ is the vector that contains the predicted values in the different simulated conditions, and ϑ is the vector that contains the model parameters that have to be identified via the model fitting. An L_2-regularisation term was added to the loss function to prevent an ill-conditioned parameter estimation problem. To keep all the model parameters within the same order of magnitude, the regularisation hyperparameter was set to $\lambda = 0.001$.

The plot in Supplementary Fig. 3 was generated in Python using the *Matplotlib* library (v. 3.5.1). The code to perform the model fitting is available publicly as a Jupyter notebook (https://github.com/giansimone/MIRELLA/).

RESULTS

A modelling framework explains the relation between gene downregulation by microRNAs and cellular resources reallocation

We previously observed that miRNA-based iFFL circuit designs can be used to reduce the resource-based coupling of two co-expressed genes, and that miRNA-driven gene downregulation is associated with increased expression of co-encoded, independent genes (1). To understand the mechanisms underlying this indirect effect on independent genes expression, we developed MIRELLA, a deterministic resource-aware model that captures the resource-constrained co-expression of two constitutive genes when one of them is downregulated by an endogenous miRNA (Figure 2A). With a focus on miRNA activity as a key player in iFFL-based burden mitigation, MIRELLA extends existing models of biochemical reactions by taking into account the effects of shared cellular resources. This is achieved through the use of effective reaction rates that depend on cellular resources demand, like previously done in (1), while explicitly accounting for ribosomes and RNases resource pools (Figure 1B). In what follows, we provide a brief overview of the model, whilst its full details can be found in Supplementary Note 1.

Since miRNAs act post-transcriptionally, the model focuses on the processes that contribute to proteins' expression, namely miRNA-dependent mRNA downregulation, mRNA degradation and mRNA translation. The driving hypothesis is that the observed increased expression of an independent gene following the downregulation of the miRNA target is likely due to the reallocation of shared cellular resources involved in post-transcriptional processes. The model thus consists of a set of ordinary differential equations (ODEs) that capture the relative gene expression levels of a constitutive gene which is modulated by an endogenous miRNA (*miTarget*—Figure 2A), and a second constitutive gene, whose expression levels reflect variations in the availability of shared cellular resources (*capacity*

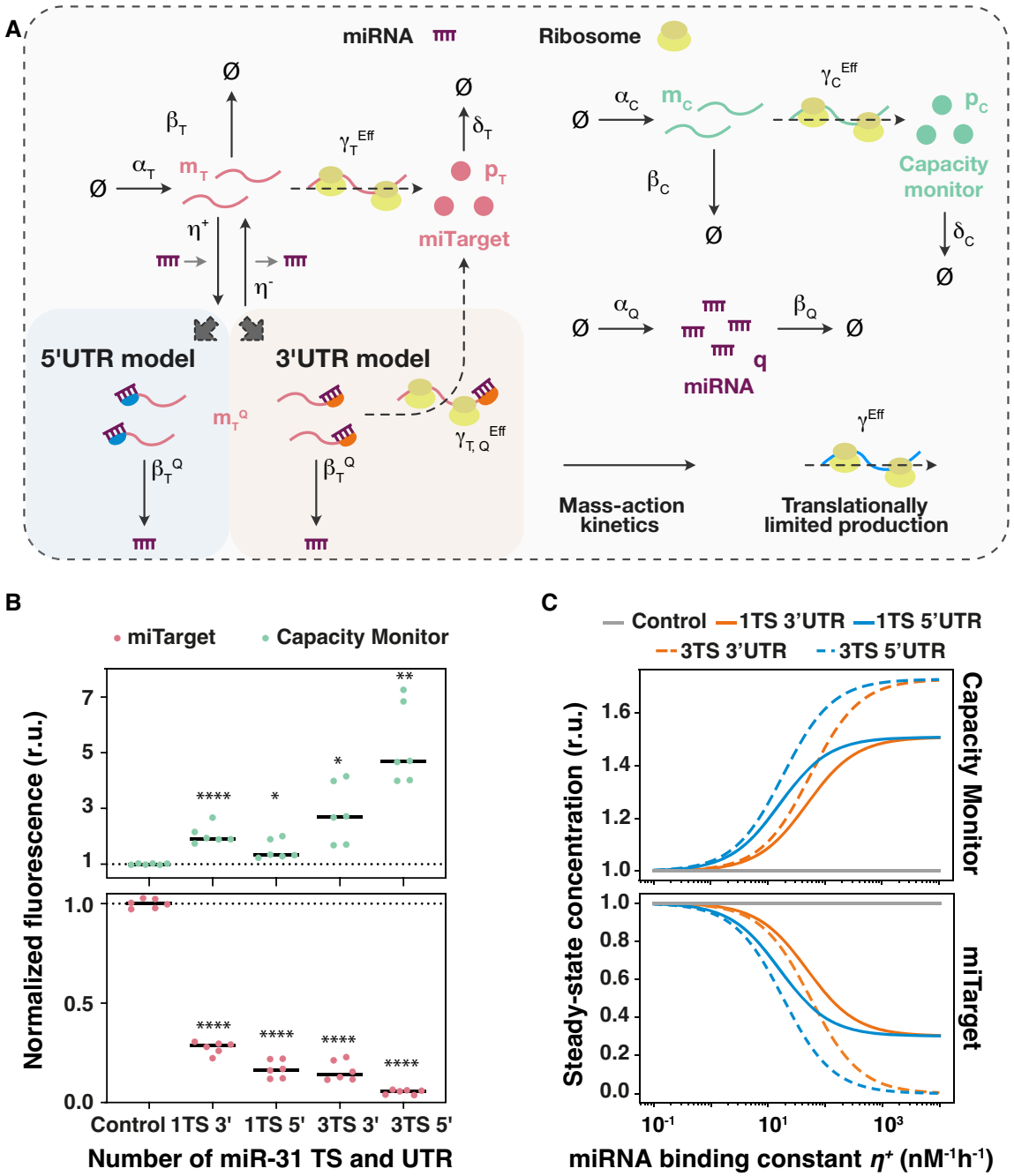

Figure 2. MIRELLA modelling framework used to capture miRNA-effect on resource allocation. (**A**) Graphical representation of the resource-aware model used to study the reallocation of the translational resources (ribosomes). For each of the two exogenous genes, the model captures the essential features of translation, degradation, and interactions between genes and ribosomes. Initially, the model does not capture the interactions between genes and RNases since the shared cellular resource pool for RNA degradation (RNases) is here considered unlimited. The competition for the shared pool of ribosomes is captured via the effective translation rate constants γ_T^{Eff} and $\gamma_{T,Q}^{Eff}$ (*miTarget*), and γ_C^{Eff} (*capacity monitor*). The miRNA mode of action changes according to the location of the miR-TS and generates two different models: the '3' UTR model' and the '5' UTR model'. The strength of the miRNA regulation is modelled via the miRNA-to-*miTarget*-mRNA binding constant η^+. (**B**) Fold change of miTarget and capacity monitor protein levels compared to control (noTS) set to 1. Flow cytometry data were acquired 48 h post-transfection and plotted as mean. r.u.: relative units. $N = 6$ biological replicates. Unpaired two-sided *t*-test. *P* value: ****<0.0001, **<0.005, *<0.05. Dataset taken from (1). (**C**) Predicted steady-state protein levels of the *miTarget* (bottom) and the *capacity monitor* (top) varying the miRNA binding constant η^+ when considering different design conditions. Each colour represents a different design condition that depends on the location and the number of the miRNA target sites within the UTRs of the *miTarget* gene, i.e. 1 or 3 TS, either in the 3' or the 5' UTR. The miRNA binding constant η^+ is considered as an independent variable and thus is not set to a fixed value. The values considered for η^+ span a range of reasonable characteristic values. r.u.: relative units. A description of the model can be found in Supplementary Notes 1–3. All the molecular species captured in the model are listed in Supplementary Table 4, whilst all the model parameters—including the numerical values used for the presented simulation results—are summarised in Supplementary Table 5.

monitor—Figure 2A). The *miTarget* is a mRNA encoding for a red fluorescent protein (mKate) that includes target sites for miR-31 in its 5' or 3' UTR, whereas the *capacity monitor* is a constitutively expressed green fluorescent reporter (EGFP). For each of these two genes, the model captures the essential features of transcription, translation, degradation, and also the interactions between genes and shared cellular resource pools as illustrated in Figure 2A. The model assumes that the shared cellular resource pool for translation (here comprising only ribosomes for simplicity) is constant, whereas the pool for RNA degradation (e.g. RNases) is initially considered unlimited. This enables us to initially neglect the demand for RNA degradation resources and to focus on how miRNA-driven regulation impacts ribosomes reallocation (Figure 2A and 3A, B). In a second step, we consider a finite pool of RNases, which are reallocated depending on degradation demand from the co-expressed genes (Figure 4A, B). Focusing on post-transcriptional events, the model does not explicitly consider shared transcriptional resource pools. This choice does not affect the results and the conclusions since variations in transcriptional burden can be accounted by a change in the transcription rate constants α_T, α_C, and α_Q as shown in Supplementary Note 2. The core elements of the model include the effective translation rate constants for both the *miTarget* (γ_T^{Eff}) and *capacity monitor* (γ_C^{Eff}) genes (Supplementary Note 1). These rates change dynamically according to the translational resource demand, which depends on the mRNA expression levels m_T and m_C, and on the effective dissociation constants κ_T and κ_C (see Supplementary Note 1 for further details). The model considers two main modes of action of miRNAs on their target genes, namely regulation of translation initiation (23,24) and mRNA degradation (25). Since synthetic circuits commonly use perfectly complementary TS to maximise the downregulation, we consider mRNA degradation the main outcome of miRNAs activity. However, when located in proximity of the AUG at the 5' UTR, we additionally consider a steric hindrance effect of miRISC complex that competes with ribosome binding and impairs mRNA translation (26) (Figure 1C).

To capture the binding interactions between the *miTarget* mRNA and its cognate miRNA, the model considers a further molecular binding reaction as illustrated in Figure 2A. The strength of the miRNA regulation is modelled via the characteristic parameter associated with the binding reaction between the *miTarget* mRNA and its cognate miRNA, that is the miRNA binding constant η^+ (Figure 2A). η^+ can be used as a proxy for capturing the effect of different repetitions of TS in the 5' or 3' UTRs of the target mRNA. Hereafter, the binding constant η^+ is assumed to be proportional to the number of TS (i.e. we do not consider cooperation effects in miRNA-driven regulation). The '3' UTR model' (shaded orange region in Figure 2aA) considers miRNA regulation via the mRNA degradation rate β_T^Q, whilst the '5' UTR model' (shaded blue region in Figure 2A) considers miRNA regulation via both the mRNA degradation rate β_T^Q and the effective translation rate $\gamma_{T,Q}^{Eff}$ (Supplementary Note 1). We assume first-order miRNA-mediated degradation of the target mRNA *miTarget*, which results in an increase of the mRNA degradation rate by a factor $\lambda_T^Q > 1$, that is $\beta_T^Q = \lambda_T^Q \times \beta_T$. When the TS are within the 5' UTR, the model assumes that the effective translation rate $\gamma_{T,Q}^{Eff}$ is equal to zero since, in this case, *miTarget:miRNA* transcripts cannot be translated due to steric hindrance.

To check if our model correctly predicts protein expression upon miRNA regulation, we ran simulations of the resource-aware model and compared the results with the experimental data published in (1). Data represent the protein levels of *miTarget* and *capacity monitor* in H1299 cells, which naturally express high levels of miR-31. *miTarget* and *capacity monitor* are under the regulation of a bidirectional constitutive CMV promoter (Supplementary Figure 9a). The *miTarget* includes either 1 or 3 TS in the 3' or in the 5' UTR. The higher the number of TS, the stronger the repression exerted by miR-31, and consequently, the higher the *capacity monitor* levels (Figure 2B).

We simulated the presence of multiple miRNA TS in both the 3' UTR and 5' UTR by considering a range of reasonable characteristic values for the miRNA binding constant η^+ (Supplementary Table 5 and Supplementary Note 6), and monitored at the steady-state the values of the molecular species of the system (Materials and Methods). Simulation results confirmed that the resource-aware model can recapitulate the steady-state protein levels of the *miTarget* and the *capacity monitor* observed in the experimental data (Figure 2C). We found that miRNA binding constant η^+ is positively correlated with the steady-state protein levels of the *capacity monitor*. As expected, the simulation results showed that when miRNA TS are located in the 5' UTR there is stronger downregulation of the *miTarget* followed by higher *capacity monitor* levels (Figure 2C).

We next solved the model analytically to obtain insights into resource demands that account for the steady-state levels of both the *miTarget* and the *capacity monitor* proteins (Eq. (1), Materials and Methods; full details in Supplementary Note 4). We found that these levels depend on the resource demand coefficients ρ_T (for *miTarget* translation, Eq. (2a)), ρ_C (for *capacity monitor* translation, Eq. (2c)), and ρ_T^Q (for *miTarget:miRNA* translation, Eq. (2b)). We noticed that the resource demand coefficient ρ_T^Q is nonzero only when TS are present in the 3'UTR (Eq. (2b)). We also observed that the miRNA regulation directly alters the resource demand coefficients associated with *miTarget* translation, although in different ways. More specifically, the coefficient ρ_T (Eq. (2a)) is downregulated by both the miRNA binding constant η^+ and the miRNA-enhanced degradation rate β_T^Q. In contrast, the demand coefficient ρ_T^Q (Eq. (2b)) is upregulated by the miRNA binding constant η^+ and downregulated by the miRNA-enhanced degradation rate β_T^Q. Therefore, the miRNA-driven *miTarget* degradation reduces the resource demand coefficients, and hence the amount of *miTarget* mRNA that is translated into *miTarget* proteins. This effect leads to a redistribution of the translational resources on the *capacity monitor* transcripts, which in turn increases the amount

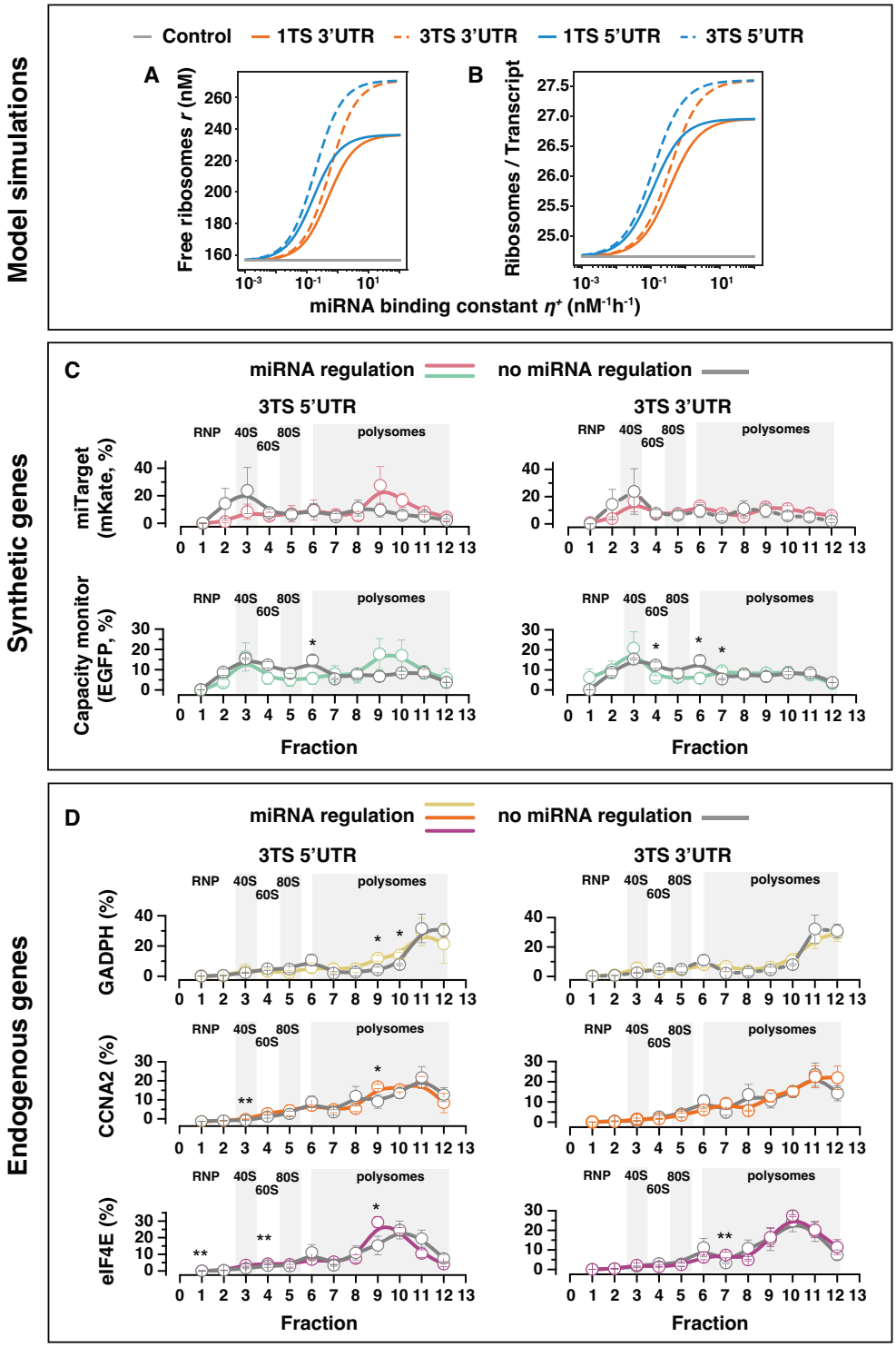

Figure 3. Ribosomes redistribution. (**A**) Predicted steady-state concentration levels of the free ribosomes varying the miRNA binding constant η^+ in different design conditions. (**B**) Predicted steady-state ribosomal densities (Materials and Methods) for both the *miTarget* and *capacity monitor* genes varying the miRNA binding constant η^+ in different design conditions. Design conditions include different location and number of the miRNA target sites within the UTRs of the *miTarget* gene. The miRNA binding constant η^+ is considered as an independent variable and thus is not set to a fixed value. Instead, the values considered for η^+ span a range of reasonable characteristic values. An increase in the miRNA binding constant η^+ is correlated to an increase in the pool of free ribosomes and the ribosomal densities, and supports the hypothesis of ribosomes reallocation upon miRNA-driven regulation. (C, D) Relative distribution of transcripts and co-sedimentation analysis in polysomes profiles in H1299 cells transfected with a bidirectional promoter plasmid encoding for EGFP (*capacity monitor*) and mKate (*miTarget*) with miR-31 TS either at the 5' or 3' UTR. As control, we used the same plasmid lacking the miR-31 target sites. We analysed both synthetic (**C**) and endogenous (**D**) genes. Polysome profiles were obtained 48 hours post transfection. Means of the relative percentage of transcript sedimentation along the profile ± SE. SE: standard errors are shown. $N = 3$ biological replicates. Unpaired two-sided *t*-test. *P*-value: * < 0.05, ** < 0.005.

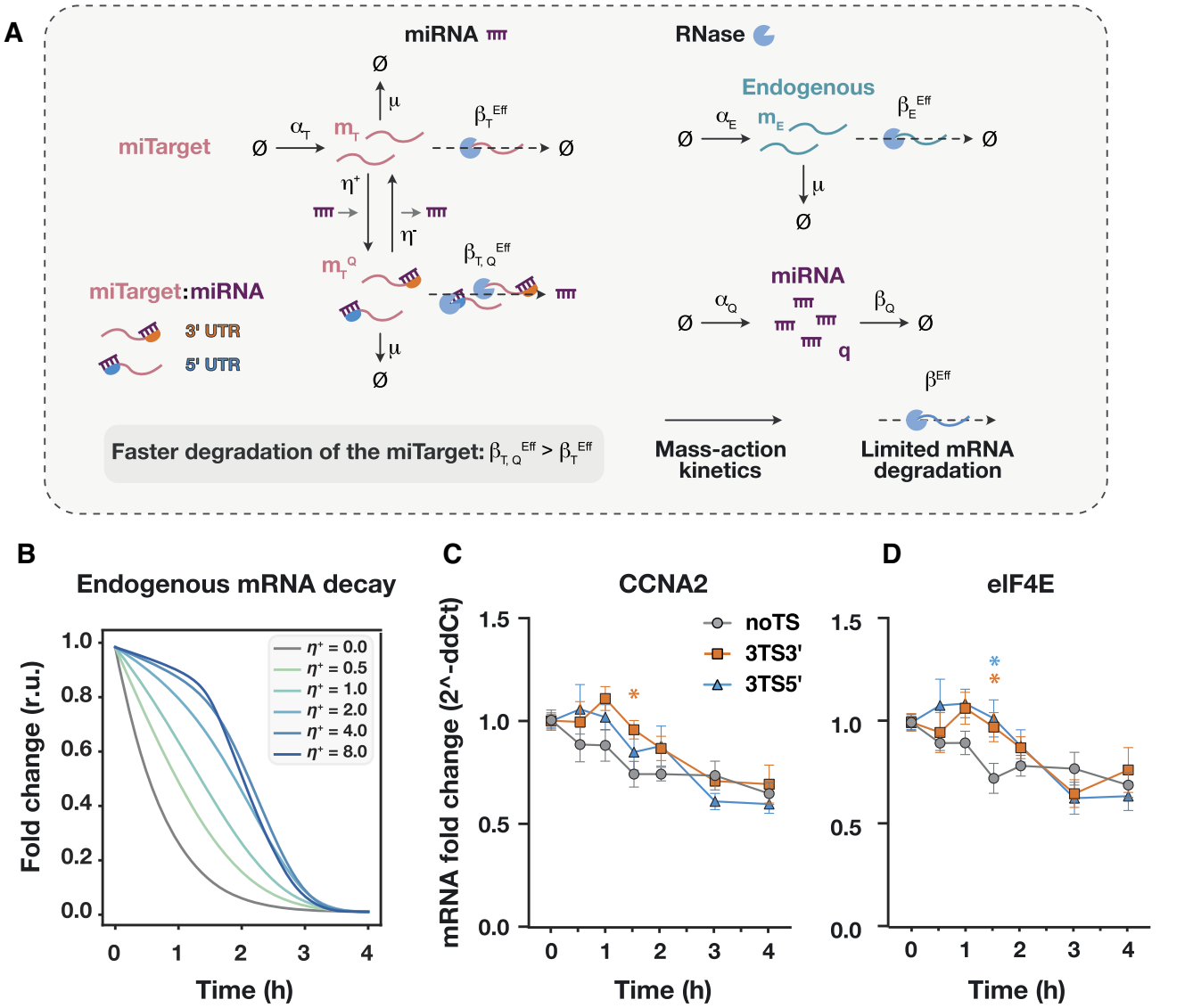

Figure 4. miRNA action increases non-target transcripts' half-life. (**A**) Graphical representation of the resource-aware model used to study the reallocation of the degradation resources (RNases). The model described in Figure 2 is extended to include a finite pool of RNases. The competition for the shared pool of RNases is captured via the effective mRNA degradation rate constants β_T^{Eff} and $\beta_{T,\,Q}^{+}$ (*miTarget*), and β_E^{Eff} (*endogenous* gene). The miRNA-driven decay increases the rate of binding between the *miTarget* transcript and the degrading resources by increasing the association constant β_T^{+} to the new value $\beta_{T,\,Q}^{+}$. A description of the model can be found in Supplementary Note 5. All the molecular species captured in the model are listed in Supplementary Table 6, whilst all the model parameters—including the numerical values used for the simulations—are summarised in Supplementary Table 7. (**B**) Predicted mRNA degradation profiles of an endogenous gene upon halting of transcription for different values of the miRNA binding constant η^+. Reallocation of degrading resources alters the endogenous mRNA degradation profile and depends on the miRNA binding constant. The mRNA degradation profiles were normalised to the initial data point. Each colour represents a different value for the miRNA binding constant η^+. r.u.: relative units. **(c, d)** mRNA half-life and degradation dynamics measurement of CCNA2 (**C**) and eIF4E (**D**) upon DRB treatment (50 μM). All data were acquired 24 hours post transfection and are plotted as mean ± SE. SE: standard error. $N = 4$–8 biological replicates. An unpaired two-sided *t*-test was used to compare 3TS3' and 3TS5' samples to the noTS control. *P*-value: * < 0.05.

of *capacity monitor* proteins. This is the only source of translational resource redistribution in the 3' UTR model, whereas the absence of the coefficient ρ_T^Q (i.e. $\rho_T^Q = 0$) when TS are present in the 5' UTR amplifies the redistribution effect in line with the experimental data shown in Figure 2B. We further validated the resource-aware model by fitting the model parameters to the experimental data as shown in Supplementary Figure 3 (Materials and Methods).

Regulation by miRNA binding to the 5'UTR results in ribosomes reallocation and modified translational profiles

To explore the effect of miRNA-driven reallocation of translational resources we first used our resource-aware model to predict the amount of free and translating ribosomes at steady state. Based on the results of the simulation reported in Figure 2C, the pool of free ribosomes positively correlates with the miRNA binding constant η^+

(Figure 3A), and with the location of miRNA-TS. Furthermore, the *ribosomal density* defined here as the number of translating ribosomes *per* total number of transcripts, positively correlates with the miRNA binding constant η^+ for both the *miTarget* and the *capacity monitor* (Figure 3B). This suggests that the miRNA-driven downregulation of the *miTarget* frees up translational resources, which can be deployed to the translation of other transcripts, including co-expressed ones such as the *capacity monitor*. We investigated what may cause the ribosomes reallocation by analytically solving the model at the steady state (Supplementary Note 4). We derived the steady-state level for the pool of free ribosomes ($\bar{r}$) and found that it is inversely proportional to the sum of the resource demand coefficients, that is $\bar{r} \sim \frac{1}{\rho_T+\rho_T^Q+\rho_C}$ (Supplementary Note 4). Since miRNA regulation does not affect the *capacity monitor* resource demand coefficient, a reduction in the total *miTarget* resource demand (i.e. $\rho_T + \rho_T^Q$) corresponds to an increase in the amount of free ribosomes (Supplementary Note 4). We then analytically calculated the steady-state ribosomal densities for the *capacity monitor* transcripts and found that these correlate with the amount of free ribosomes (Supplementary Note 4). Of note, our simulations and the analytical solution show an increased number of ribosomes per transcript also for the *miTarget* mRNA when the miR-TS are located at the 5' UTR (Figure 3B, Supplementary Note 4). Even if counterintuitive, this suggests that the increased amount of available ribosomes is to the benefit of *miTarget* transcripts that did not undergo miRNA-mediated downregulation.

Next, we experimentally validated the model predictions. We performed polysome profiling in H1299 cells transfected with *miTarget* and *capacity monitor* to observe the changes in co-sedimentation of the reporter mRNAs with polysomes (19,20) following miRNA modulation. We considered several conditions, including no miRNA regulation and TS inserted in the 5' or 3' UTR (Figure 3C, D). After sucrose gradient separation of cytoplasmic lysates, it is possible to follow the sedimentation of transcripts with free cytosolic light components (ribonucleoproteins, RNPs), ribosomal subunits (40S and 60S) and monosomes (80S) - all associated with non-translating particles - and with polysomes comprising translating transcripts bound by multiple ribosomes (Figure 3C, D). In line with model predictions, both the *capacity monitor* (EGFP, Figure 3C, bottom) and the *miTarget* (mKate, Figure 3C, top) exhibit modified co-sedimentation profiles upon miR-31 modulation as compared to the control (no miRNA regulation, grey line). In addition, we monitored the co-sedimentation profiles of endogenous transcripts, i.e. eIF4E, CCNA2 and GAPDH, that we previously observed to be impacted by resource competition. Following miRNA regulation of *miTarget,* we found that they also benefit from ribosome reallocation (Figure 3D). Our data indicate that for all analysed genes, there is a shift towards the polysomal fractions (peaks 9–10) that is more pronounced when the miR-31 TS are placed at the 5' UTR (Figure 3C, D, left) as compared to the 3' UTR (Figure 3C, D, right) of the *miTarget*. These results are consistent with our hypothesis stating that, due to the physical proximity of the TS to the AUG, the miRISC complex interferes with the binding of ribosomes to the target mRNA, resulting in their re-allocation on other transcripts.

microRNA activity induces a queuing effect on mRNA degradation

Along with ribosome redistribution, we used MIRELLA to investigate the impact of miRNA-driven regulation on the RNA degradation machinery. To this end, we modified our model to include a finite pool of RNases (Supplementary Note 5), recapitulating the essential features of transcription, degradation, and interactions between transcripts and the degrading resource pool (RNases) as illustrated in Figure 4A. We then simulated the degradation of an *endogenous* transcript upon halting of transcription (i.e. all transcription rate constants were set to zero after the system reached its steady state) for different reasonable values of the miRNA binding constant η^+ (Supplementary Table 7 and Supplementary Note 6).

The competition for the shared pool of RNases is captured via the effective mRNA degradation rates derived for the *miTarget* (β_T^{Eff}) and the *endogenous* (β_E^{Eff}) gene (Figure 4A and Supplementary Note 5). The effective degradation rates approximate the degradation reactions shown in Supplementary Fig. 2 with simpler first-order decay reactions (Figure 4A and Supplementary Note 5). These rates change dynamically and depend both on the expression levels of the degrading *mRNA:RNase* complexes (s_T and s_E, Supplementary Fig. 2) and the association and dissociation constants between the RNase and the mRNA strands (Supplementary Note 5 for further details). We assume that the miRNA-driven decay increases the rate of binding between the *miTarget* transcript and the molecular species of the degradation machinery by increasing the association constant β_T^+ to the new value $\beta_{T,\,Q}^+$ (Supplementary Fig. 2). This effect produces an increase in the effective mRNA degradation rate β_T^{Eff} to the new value $\beta_{T,\,Q}^{Eff}$ (Figure 4a). The model predicted an altered degradation profile depending on the miRNA binding constant η^+ (Figure 4B, extended data presented in Supplementary Fig. 4) and showed that the endogenous degradation dynamics are slower when compared to the control ($\eta^+ = 0$). Moreover, the endogenous degradation profile presents two different decay phases when the miRNA binding constant η^+ is greater than $\sim 2\ \mathrm{nM}^{-1}\ \mathrm{h}^{-1}$ (Figure 4B and Supplementary Figure 4b). Specifically, the endogenous mRNA levels remain almost stable during the first decay phase, whereas they degrade quicker during the second phase. We hypothesise that the increased degradation of the target by miR-31 (Supplementary Figure 4a) sequesters a significant portion of the degradation machinery (Supplementary Fig. 4c, d), which is thus not available for the degradation of non-target mRNAs (Figure 4A and Supplementary Figure 4b, e). We also observed that the decay dynamics of the non-targeted transcripts become faster once the majority of *miTarget* transcripts are degraded (Supplementary Figures 4 and 5), probably due to the reallocation of degrading resources from the *miTarget* mRNAs to the non-target mRNAs (Supplementary Figure 4d, e).

To experimentally validate the model predictions, we treated cells with 5,6-dichloro-1-beta-D-ribobenzimidazole (DRB), a transcription inhibitor (27) and measured the mRNA half-life of the endogenous genes CCNA2 and eIF4E, whose half-life are reported within the range 2–4 h (28) (Figure 4C, D). We selected these genes since their mRNA half-life is much shorter than that of the *capacity monitor* EGFP, which is roughly >8 h (29) and thus does not permit to capture faster decay dynamics.

We transfected H1299 cells with mKate encoding plasmid with noTS or 3 miR-31 TS at either the 3' or the 5'UTR along with a constitutively expressed EGFP. Over a timeframe of 4 h, CCNA2 and eIF4E mRNAs exhibit a longer decay time when mKate is flanked by miR-31 TS as compared to the control (no miR-31 TS) (Figure 4C, D). More specifically, the two mRNA species decrease immediately after treatment only in the control, while in the case of 3TS at the 3' and 5' UTRs, they remain almost stable for 1 h 30 min after treatment, undergoing a significant decrease after 2–3 h. The qualitative trend of the 3TS 3' and 3TS 5' samples are very similar and in agreement with our hypothesis that miRNAs enhance target degradation at the same rate when they bind to 3'- or 5'-UTR TS. Finally, the experimental measurements show that the two mRNA species reach a plateau 4 h post-DRB treatment, in agreement with the model predictions. Although the predicted and experimental decays exhibit the same dynamics, we find that the endogenous mRNAs are not completely degraded upon treatment with DRB, which we argue is a limitation of the mRNA half-life assay. In fact, we measured CCNA2 and eIF4E mRNAs up to 6 h post-DRB treatment in wild-type cells and observed that it reaches about 50% of the initial concentration for both genes (Supplementary Figure 8). Overall, our results confirm the model predictions and are in agreement with our hypothesis of a prominent queuing effect on the mRNA degradation pathway as a consequence of the increased degradation of the *miTarget* by miR-31.

DISCUSSION

miRNAs are fundamental building blocks of post-transcriptional control of gene expression and help to finely control genetic circuits and precisely regulate endogenous pathways. We observed that when a synthetic transcript is downregulated by an endogenous miRNA, a synthetic co-expressed mRNA is indirectly upregulated. Here, we combined mathematical modelling and experimental analysis to understand important mechanisms underlying the effect of miRNAs on resource allocation in mammalian cells, when their regulation is embedded in synthetic circuits. This understanding is instrumental to generate more detailed guidelines for an informed and rational design of gene circuits, and may also provide insights into endogenous gene regulation.

We had previously observed that exogenous genes delivered in mammalian cells compete for intracellular resources. This effect was observed, albeit to a different extent, regardless of genes amount and cell types (1).

Since miRNAs function at post-transcriptional level, we developed a mathematical model, MIRELLA, that considers effective reaction rates of biological processes to account for the availability of post-transcriptional shared resources. Specifically, the model considers one pool of mRNA translation resources and one pool of mRNA degradation resources, for simplicity represented by ribosomes and RNases, respectively (Figures 2A and 4A). Although the aforementioned biological processes are regulated by many molecular species, the key cause of resource competition in mammalian cells still remains an open question. Here we focused on ribosomes and RNases for their relevance in these processes and—relatively to ribosomes—for the possibility to experimentally measure them. This allows us to keep the model as simple as possible to study the role of two prime contributors—that is ribosomes and RNases—in gene expression burden. We anticipate that other molecular species could contribute to shaping gene expression as a result of resource competition, such as tRNAs for rare codons in mRNA translation. In this respect, our resource-aware modelling framework can be extended to capture more complex scenarios, for example, by including the resource competition for shared tRNAs in the model's equations. Moreover, our context-aware theory paves the way towards a holistic understanding of cell biology (30) instrumental to engineer more sophisticated biomolecular circuits that can maximise the global system's output (e.g. a protein or a compound of interest) by operating synergistically with the cell physiology (31)

The experimental setting is based on two fluorescent reporters driven by constitutive promoters, one regulated by an endogenous miRNA (*miTarget*) and the other lacking regulation, as a proxy for resources availability (*capacity monitor*). This design is simple and is meant to quickly appreciate differences in protein expression levels. The modelling framework suggested that miRNA regulation has two major consequences on resource allocation. One is a queueing effect on the RNA degradation pathway as the result of the strong miRNA-mediated slicing of *miTarget* transcripts. The other is an increased amount of ribosomes becoming available for translating other transcripts.

Synthetic networks that embed miRNA regulation typically employ perfectly complementary TS to maximise the fold change expression of the target gene (18), and it has been generally observed that the abundance of miRNAs with respect to their target affects genetic circuits functionality (32). It was previously proposed that a significant mRNA degradation by miRNA may lead to a 'queueing effect' for the degradation of other mRNAs, decreasing the effective mRNA decay rate (33). We validated this hypothesis by quantifying the mRNA decay of two endogenous genes, CCNA2 and eIF4E, which were previously shown to be impacted by the burden imposed by the expression of synthetic circuits (1). We observed that upon transcription-inhibition treatment with DRB, CCNA2 and eIF4E are degraded at a slower pace in the samples expressing *miTarget* as compared to the control lacking the TS. These results suggest that an accumulation of other mRNAs contributes to increased cognate protein levels. This finding may be useful for circuit design considerations, particularly when such systems are devised to study endogenous processes or pathways.

Our experimental findings suggest that ribosomes reallocate upon miRNA regulation and that this effect is more

pronounced when miRNA-TS are located in the 5'UTR of the target gene. We speculate that the proximity of TS to the AUG may prevent ribosomes from binding due to steric hindrance, effectively reducing the translation of the transcript. It was previously observed that miRNA-RISC may decrease the rate of translation initiation (25). One mechanism reported that Argonaute proteins, along with miRNA and cognate targets accumulate in P-bodies in a miRNA-dependent manner (23,24,34,35), increasing the amount of ribosome-free mRNA and free ribosomes. Our model also suggested that the downregulation of the *miTarget* would result in more free ribosomes. Therefore, we performed polysome profiling to observe changes in the co-sedimentation profiles of transcripts with ribosomes in polysomes. Of note, a modified co-sedimentation profile of the *capacity monitor,* with a shift towards heavier gradient fractions (9–10, Figure 3C) in the 5'UTR-TS condition was expected. In contrast, the altered profile of the *miTarget* was surprising. In contrast, a previous study reported that translation repression by Let-7 miRNA in mammalian cells resulted in a shift of the mRNA target to lighter fractions in polysome gradients (24). We speculate that our system differs in TS location (5' versus 3'UTR) and complementarity (perfect *vs* non-perfect) from the abovementioned study. Therefore, since there is a major effect of *miTarget* degradation due to the endonuclease activity of the miRISC complex, there is an enrichment of the remaining transcripts with the available ribosomes, including the *miTarget* transcripts escaping the miRNA activity. This speculation was supported also by our MIRELLA model. Regardless of *where* ribosomes reallocate, it is important to consider this secondary effect of miRNA regulation. The primary function of miRNAs is the downregulation of the target genes, and recently other properties of miRNA were demonstrated, such as buffering gene expression against noise or external inducer concentration (10–12). Our results indicate further hidden secondary effects that could play a role in the general homeostasis of protein expression. However, proving this idea in an endogenous system is challenging since miRNAs are embedded in intricate networks that do not allow to untangle single effects of miRNA regulation easily. In future studies, it could be interesting to analyse the impact of miRNAs on resource allocation as related to the number of ribosomes sequestered by the *miTarget*. This could be achieved by placing internal ribosome entry sites (IRES) in the target transcript and observing the effect on the *capacity monitor* once the miRNA activity is impaired (e.g. by miRNA-specific inhibitors).

Resource competition can dramatically affect circuits behaviour and cellular physiology. Conversely, burden mitigation can speed up the cumbersome design-build-test cycle and open up avenues for the predictive design and engineering of more reliable gene constructs in mammalian cells. In this respect, our study provides the scientific community with a necessary understanding for robustly and effectively building genetic devices and biomolecular controllers—for example, iFFL architectures based on miRNAs (1,36)—that rely on precise quantitative assessment of molecular species. Our study also highlights that the use of appropriate experimental controls for a desired genetic circuit architecture, along with appropriate computational tools may be key to avoid results misinterpretation and to correctly predict the overall outcome of the synthetic device. Moreover, our results contribute to compelling insights into primary and secondary regulatory effects of miRNA action with implications for basic science and for industrial and medical biotechnology.

DATA AVAILABILITY

The source code that supports the findings of this study is available publicly from GitHub at https://github.com/giansimone/MIRELLA/ (DOI: 10.6084/m9.figshare.21725387). The data underlying this article are available in the article and in its online supplementary material (SourceData).

SUPPLEMENTARY DATA

Supplementary Data are available at NAR Online.

ACKNOWLEDGEMENTS

We thank Daniela Perna for technical support. We also thank the RNA initiative at IIT for scientific inputs.
Author contributions: F.C. and V.S. conceived the project and designed experiments. F.C. and G.V. performed polysome profiling. F.C. and F.T. performed DRB experiments. F.C., G.V. and F.T. performed data analysis. G.P. and GB.S. developed the mathematical model. C.B. provided inputs on the mathematical model. V.S. supervised the experimental work and secured funding. G.B.S. supervised the computational work and secured funding. F.C., G.P. and V.S. wrote the manuscript. GB.S. and F.T. edited the manuscript.

FUNDING

ERC Starting grant Synthetic T-rex [852012]; NextGenerationEU PNRR MUR [M4C2]; National Center for Gene Therapy and Drugsbased on RNA Technology [CN00000041]. Funding for open access charge: Stan lab. GB.S. acknowledges funding from the Royal Academy of Engineering through the RAE Chair in Emerging Technologies programme (RAEng CiET 1819\5).
Conflict of interest statement. None declared.

REFERENCES

1. Frei,T., Cella,F., Tedeschi,F., Gutiérrez,J., Stan,G.-B., Khammash,M. and Siciliano,V. (2020) Characterization and mitigation of gene expression burden in mammalian cells. *Nat. Commun.*, **11**, 4641.
2. Jones,R.D., Qian,Y., Siciliano,V., DiAndreth,B., Huh,J., Weiss,R. and Del Vecchio,D. (2020) An endoribonuclease-based feedforward controller for decoupling resource-limited genetic modules in mammalian cells. *Nat. Commun.*, **11**, 5690.
3. Shakiba,N., Jones,R.D., Weiss,R. and Del Vecchio,D. (2021) Context-aware synthetic biology by controller design: engineering the mammalian cell. *Cell Syst.*, **12**, 561–592.
4. Boo,A., Ellis,T. and Stan,G.-B. (2019) Host-aware synthetic biology. *Curr. Opin. Syst. Biol.*, **14**, 66–72.
5. Fabian,M.R., Sonenberg,N. and Filipowicz,W. (2010) Regulation of mRNA translation and stability by microRNAs. *Annu. Rev. Biochem.*, **79**, 351–379.

6. Saito,H., Kobayashi,T., Hara,T., Fujita,Y., Hayashi,K., Furushima,R. and Inoue,T. (2010) Synthetic translational regulation by an L7Ae-kink-turn RNP switch. *Nat. Chem. Biol.*, **6**, 71–78.
7. O'Brien,J., Hayder,H., Zayed,Y. and Peng,C. (2018) Overview of microRNA biogenesis, mechanisms of actions, and circulation. *Front. Endocrinol.***9**, 402.
8. Ameres,S.L., Horwich,M.D., Hung,J.-H., Xu,J., Ghildiyal,M., Weng,Z. and Zamore,P.D. (2010) Target RNA-directed trimming and tailing of small silencing RNAs. *Science*, **328**, 1534–1539.
9. Jo,M.H., Shin,S., Jung,S.-R., Kim,E., Song,J.-J. and Hohng,S. (2015) Human argonaute 2 has diverse reaction pathways on target RNAs. *Mol. Cell*, **59**, 117–124.
10. Siciliano,V., Garzilli,I., Fracassi,C., Criscuolo,S., Ventre,S. and di Bernardo,D. (2013) MiRNAs confer phenotypic robustness to gene networks by suppressing biological noise. *Nat. Commun.*, **4**, 2364.
11. Strovas,T.J., Rosenberg,A.B., Kuypers,B.E., Muscat,R.A. and Seelig,G. (2014) MicroRNA-based single-gene circuits buffer protein synthesis rates against perturbations. *ACS Synth. Biol.*, **3**, 324–331.
12. Osella,M., Bosia,C., Corá,D. and Caselle,M. (2011) The role of incoherent microRNA-mediated feedforward loops in noise buffering. *PLoS Comput. Biol.*, **7**, e1001101.
13. Carignano,A., Mukherjee,S., Singh,A. and Seelig,G. (2018) Extrinsic Noise Suppression in MicroRNA Mediated Incoherent Feedforward Loops. In: *2018 IEEE Conference on Decision and Control (CDC)*. IEEE, Miami, FL, USA, pp. 4353–4359.
14. Xie,Z., Wroblewska,L., Prochazka,L., Weiss,R. and Benenson,Y. (2011) Multi-input RNAi-based logic circuit for identification of specific cancer cells. *Science*, **333**, 1307–1311.
15. Miki,K., Endo,K., Takahashi,S., Funakoshi,S., Takei,I., Katayama,S., Toyoda,T., Kotaka,M., Takaki,T., Umeda,M. *et al.* (2015) Efficient detection and purification of cell populations using synthetic microRNA switches. *Cell Stem Cell*, **16**, 699–711.
16. Cella,F., Wroblewska,L., Weiss,R. and Siciliano,V. (2018) Engineering protein-protein devices for multilayered regulation of mRNA translation using orthogonal proteases in mammalian cells. *Nat. Commun.*, **9**, 4392.
17. DiAndreth,B., Wauford,N., Hu,E., Palacios,S. and Weiss,R. (2022) PERSIST platform provides programmable RNA regulation using CRISPR endoRNases. *Nat. Commun.*, **13**, 2582.
18. Gam,J.J., Babb,J. and Weiss,R. (2018) A mixed antagonistic/synergistic miRNA repression model enables accurate predictions of multi-input miRNA sensor activity. *Nat. Commun.*, **9**, 2430.
19. Lunelli,L., Bernabò,P., Bolner,A., Vaghi,V., Marchioretto,M. and Viero,G. (2016) Peering at brain polysomes with atomic force microscopy. *J. Vis. Exp.*, **109**, e53851.
20. Bernabò,P., Tebaldi,T., Groen,E.J.N., Lane,F.M., Perenthaler,E., Mattedi,F., Newbery,H.J., Zhou,H., Zuccotti,P., Potrich,V. *et al.* (2017) In vivo translatome profiling in spinal muscular atrophy reveals a role for SMN protein in ribosome biology. *Cell Rep*, **21**, 953–965.
21. Tebaldi,T., Re,A., Viero,G., Pegoretti,I., Passerini,A., Blanzieri,E. and Quattrone,A. (2012) Widespread uncoupling between transcriptome and translatome variations after a stimulus in mammalian cells. *BMC Genomics*, **13**, 220.
22. Darnell,J.C., Van Driesche,S.J., Zhang,C., Hung,K.Y.S., Mele,A., Fraser,C.E., Stone,E.F., Chen,C., Fak,J.J., Chi,S.W. *et al.* (2011) FMRP stalls ribosomal translocation on mRNAs linked to synaptic function and autism. *Cell*, **146**, 247–261.
23. Liu,J., Rivas,F.V., Wohlschlegel,J., Yates,J.R., Parker,R. and Hannon,G.J. (2005) A role for the P-body component GW182 in microRNA function. *Nat. Cell Biol.*, **7**, 1261–1266.
24. Pillai,R.S., Bhattacharyya,S.N., Artus,C.G., Zoller,T., Cougot,N., Basyuk,E., Bertrand,E. and Filipowicz,W. (2005) Inhibition of translational initiation by Let-7 MicroRNA in human cells. *Science*, **309**, 1573–1576.
25. Valencia-Sanchez,M.A., Liu,J., Hannon,G.J. and Parker,R. (2006) Control of translation and mRNA degradation by miRNAs and siRNAs. *Genes Dev.*, **20**, 515–524.
26. Gu,S., Jin,L., Zhang,F., Sarnow,P. and Kay,M.A. (2009) Biological basis for restriction of microRNA targets to the 3' untranslated region in mammalian mRNAs. *Nat. Struct. Mol. Biol.*, **16**, 144–150.
27. Bensaude,O. (2011) Inhibiting eukaryotic transcription. Which compound to choose? How to evaluate its activity?*Transcription*, **2**, 103–108.
28. Yang,E., van Nimwegen,E., Zavolan,M., Rajewsky,N., Schroeder,M., Magnasco,M. and Darnell,J.E. Jr (2003) Decay rates of human mRNAs: correlation with functional characteristics and sequence attributes. *Genome Res*, **13**, 1863–1872.
29. Sacchetti,A., El Sewedy,T., Nasr,A.F. and Alberti,S. (2001) Efficient GFP mutations profoundly affect mRNA transcription and translation rates. *FEBS Lett.*, **492**, 151–155.
30. Marucci,L., Barberis,M., Karr,J., Ray,O., Race,P.R., de Souza Andrade,M., Grierson,C., Hoffmann,S.A., Landon,S., Rech,E. *et al.* (2020) Computer-aided whole-cell design: taking a holistic approach by integrating synthetic with systems biology. *Front. Bioeng. Biotechnol.*, **8**, 942.
31. Contreras-Llano,L.E., Meyer,C., Liu,Y., Sarker,M., Lim,S., Longo,M.L. and Tan,C. (2020) Holistic engineering of cell-free systems through proteome-reprogramming synthetic circuits. *Nat. Commun.*, **11**, 3138.
32. Quarton,T., Ehrhardt,K., Lee,J., Kannan,S., Li,Y., Ma,L. and Bleris,L. (2018) Mapping the operational landscape of microRNAs in synthetic gene circuits. *NPJ Syst. Biol. Appl.*, **4**, 6.
33. Gambardella,G., Carissimo,A., Chen,A., Cutillo,L., Nowakowski,T.J., di Bernardo,D. and Blelloch,R. (2017) The impact of microRNAs on transcriptional heterogeneity and gene co-expression across single embryonic stem cells. *Nat. Commun.*, **8**, 14126.
34. Jakymiw,A., Lian,S., Eystathioy,T., Li,S., Satoh,M., Hamel,J.C., Fritzler,M.J. and Chan,E.K.L. (2005) Disruption of GW bodies impairs mammalian RNA interference. *Nat. Cell Biol.*, **7**, 1267–1274.
35. Sen,G.L. and Blau,H.M. (2005) Argonaute 2/RISC resides in sites of mammalian mRNA decay known as cytoplasmic bodies. *Nat. Cell Biol.*, **7**, 633–636.
36. Bleris,L., Xie,Z., Glass,D., Adadey,A., Sontag,E. and Benenson,Y. (2011) Synthetic incoherent feedforward circuits show adaptation to the amount of their genetic template. *Mol. Syst. Biol.*, **7**, 519.

Supplementary Information

MIRELLA: a mathematical model explains the effect of MIcroRNA-mediated synthetic genes REgulation on intracellular resource aLLocAtion

Authors:
Federica Cella[§1,7], Giansimone Perrino[§3], Fabiana Tedeschi[1,2], Gabriella Viero[4], Carla Bosia[5,6], Guy-Bart Stan*[3], Velia Siciliano*[1].

[1] Istituto Italiano di Tecnologia-IIT, Largo Barsanti e Matteucci, Naples ITA
[2] University of Naples Federico II, Naples ITA
[3] Department of Bioengineering and Centre of Excellence in Synthetic Biology, Imperial College London, U.K.
[4] Institute of Biophysics, CNR Trento, Povo, ITA
[5] Department of Applied Science and Technology, Politecnico di Torino, Torino, ITA
[6] Italian Institute for Genomic Medicine, c/o IRCCS, Candiolo, Italy.
[§] Equal contribution
[7] Present address: Department of Biosystems Science and Engineering (D-BSSE), ETH Zürich, Mattenstrasse 26, Basel, 4058, Switzerland

* Correspondence should be sent to Guy-Bart Stan (g.stan@imperial.ac.uk) and Velia Siciliano (velia.siciliano@iit.it)

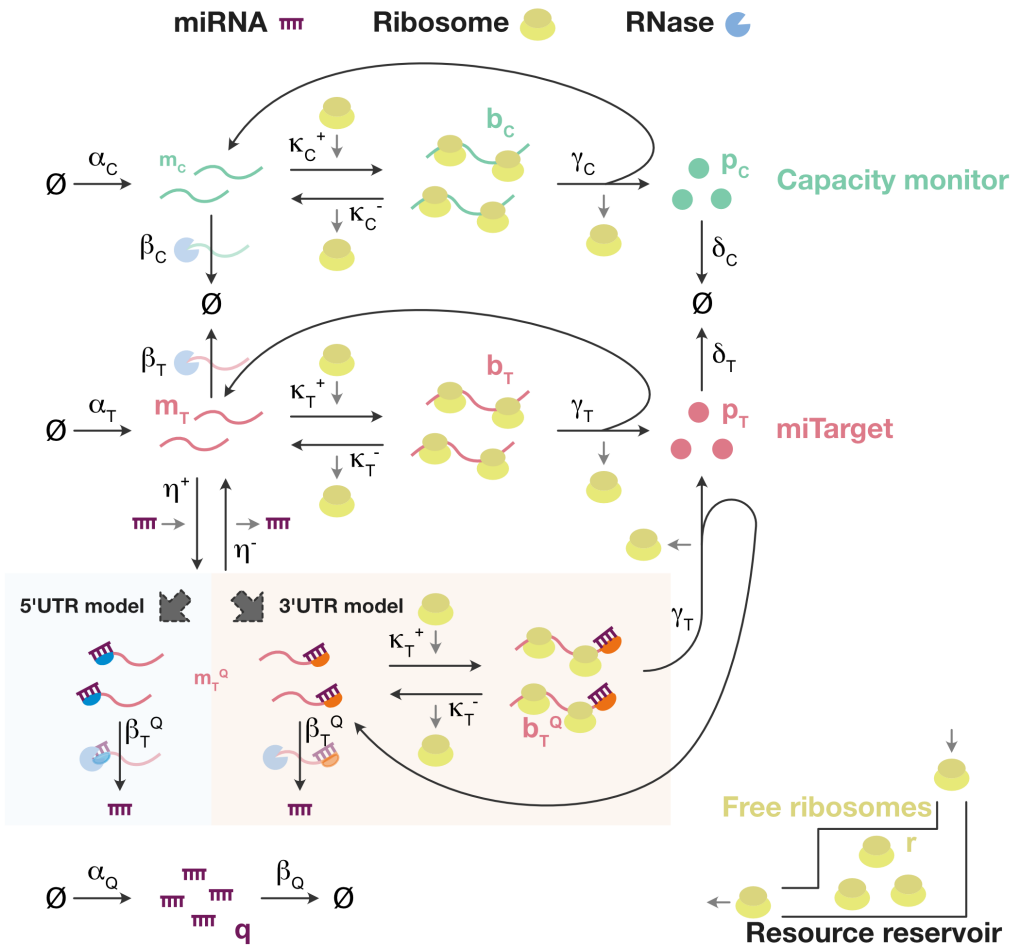

Supplementary Figure 1. Extended graphical representation of the model used to study the reallocation of the translational resources (ribosomes). Full schematics of the model used to study ribosomes reallocation caused by miRNA-driven regulation of an exogenous two-gene circuit in H1299 cells. For each of the two exogenous genes, the model captures the essential features of transcription, translation, degradation, and interactions between genes and ribosomes. The shared cellular resource pool for RNA degradation (RNases) is here considered unlimited. An exhaustive description of the model can be found in **Supplementary Notes 1-3**. All the molecular species captured in the model are listed in **Supplementary Table 4**, whilst all the model parameters – including the numerical values used for the simulations – are summarised in **Supplementary Table 5**.

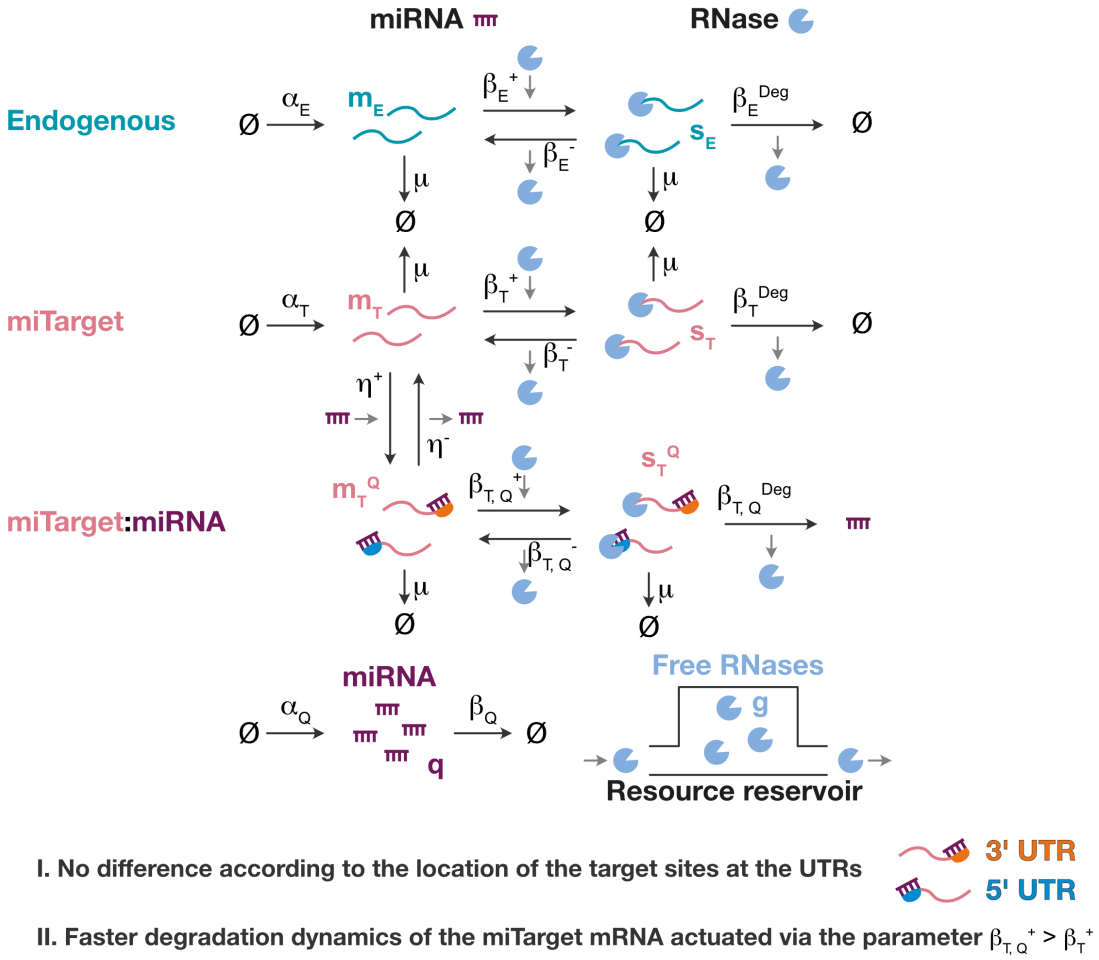

Supplementary Figure 2. Extended graphical representation of the model used to study the reallocation of the degradation resources (e.g. RNases). The model depicted in **Fig. 2a** and **Supplementary Fig. 1** is extended to include a finite pool of RNases. With this assumption, the model recapitulates the essential features of transcription, degradation, and interactions between genes and RNases. An exhaustive description of the model can be found in **Supplementary Note 5**. All the molecular species captured in the model are listed in **Supplementary Table 6**, whilst all the model parameters – including the numerical values used for the simulations – are summarised in **Supplementary Table 7**.

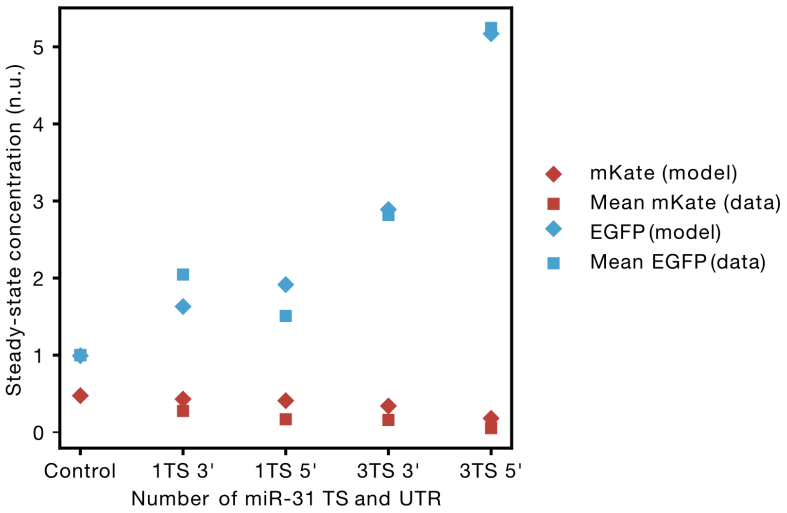

Supplementary Figure 3. Model fitting related to the experimental data shown in Fig. 2b. The ODE framework shown in **Fig. 2a** was applied to model the steady-state experimental data (squares) shown in **Fig. 2b** (**Methods**). A description of the model can be found in **Supplementary Notes 1-3**. All the molecular species captured in the model are listed in **Supplementary Table 4**. The experimental data are presented as mean values.

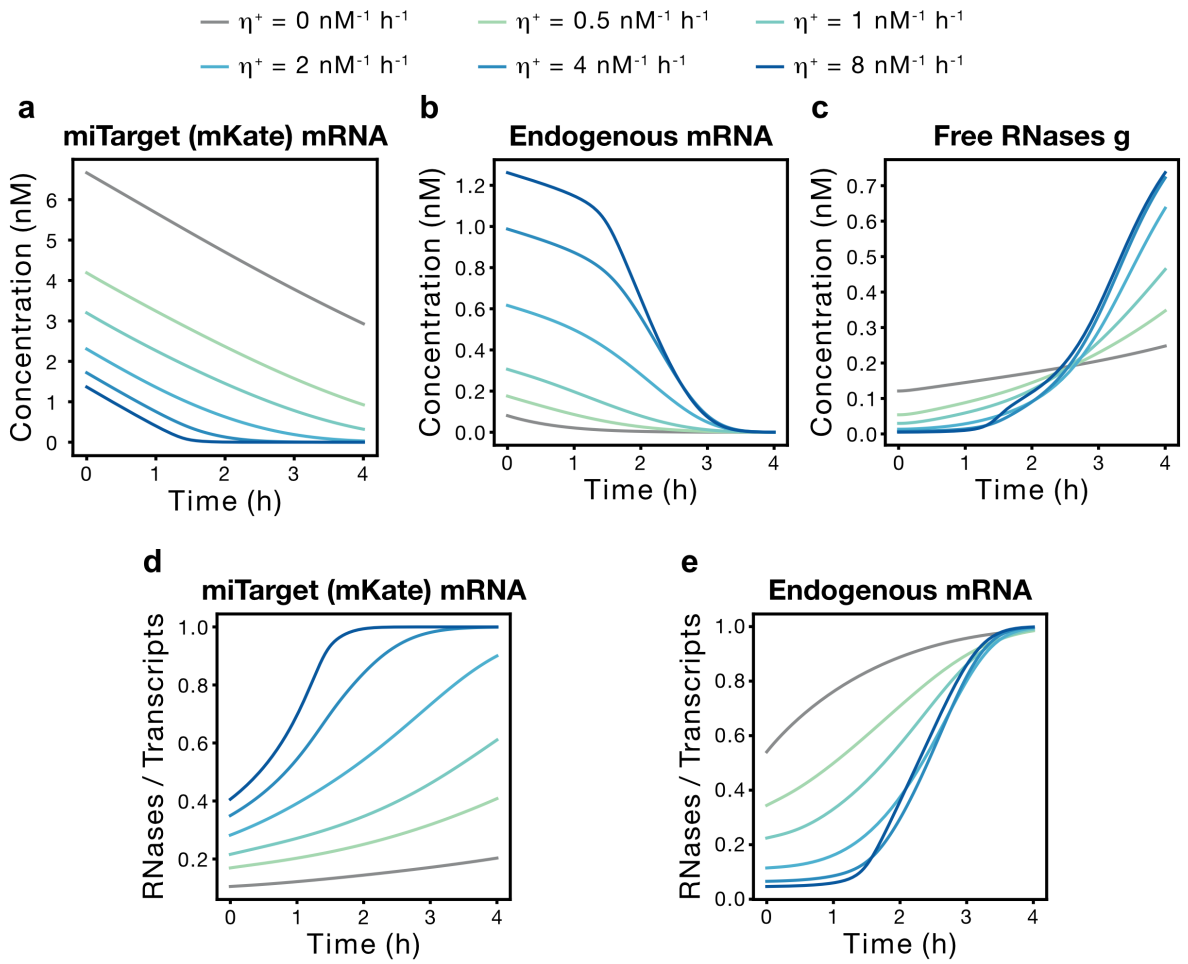

Supplementary Figure 4. Extended simulation data for Fig. 4b. (**a, b**) Predicted mRNA degradation profiles for the *miTarget* (**a**) and the endogenous gene (**b**) upon halting of transcription for different values of the miRNA binding constant η^+. (**c**) Predicted reallocation profiles for the RNases (i.e., degrading resource) for different values of the miRNA binding constant η^+. (**d, e**) Predicted degrading resource densities (i.e., RNases/transcripts) for the *miTarget* (**d**) and the endogenous gene (**e**). Each colour represents a different value for the miRNA binding constant η^+. A description of the model can be found in **Supplementary Note 5**. All the molecular species captured in the model are listed in **Supplementary Table 6**, whilst all the model parameters – including the numerical values used for the simulations – are summarised in **Supplementary Table 7**.

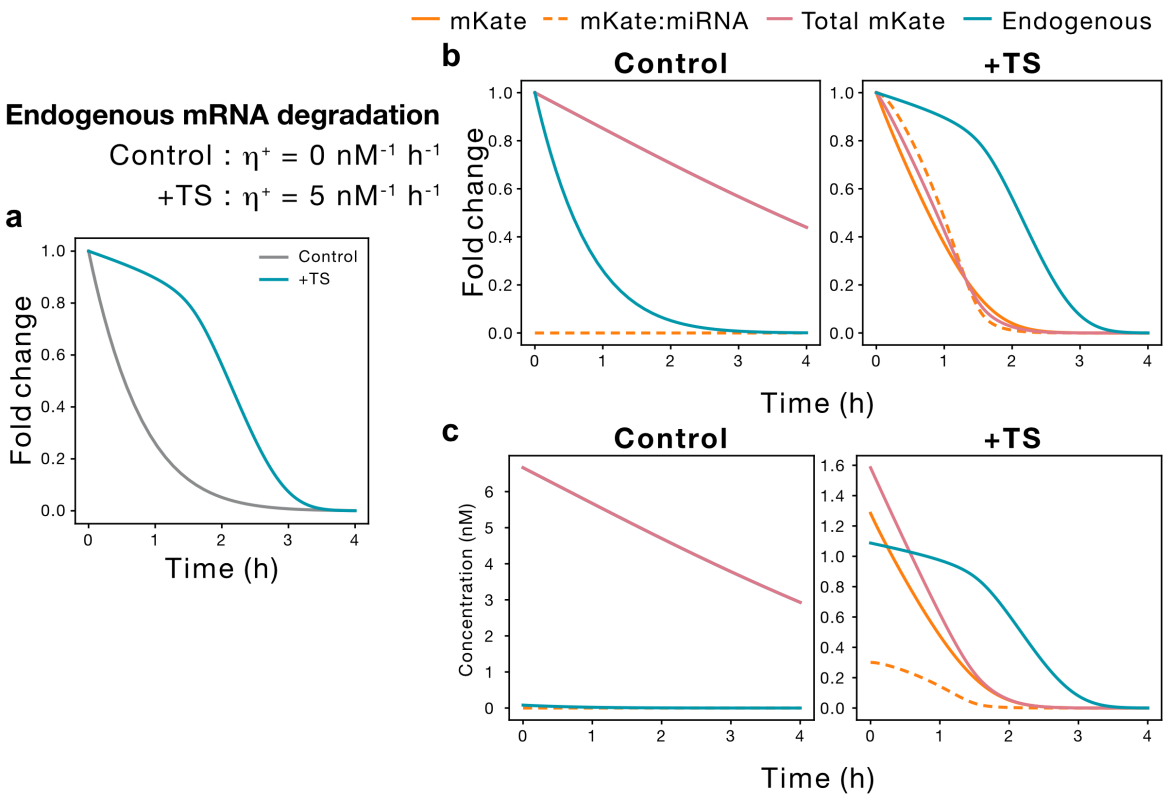

Supplementary Figure 5. Example of an endogenous mRNA decay with and without reallocation of the shared degrading resource pool. (**a**) Predicted fold change for the mRNA degradation profiles of an endogenous gene upon halting of transcription with (+TS) and without (Control) miR-TS at the UTRs of the *miTarget* gene. (**b**) Predicted fold change for the mRNA decay profiles of all mRNA species involved in the model upon halting of transcription with and without miR-TS at the UTRs of the *miTarget* (mKate) gene. (**c**) Predicted mRNA expression levels for all mRNA species involved in the model upon halting of transcription with and without miR-TS at the UTRs of the *miTarget* (mKate) gene. The model predicts an impairment of the endogenous mRNA decay upon miRNA-driven regulation that is caused by a reallocation of the RNases on the exogenous *miTarget* gene. A description of the model can be found in **Supplementary Note 5**. All the molecular species captured in the model are listed in **Supplementary Table 6**, whilst all the model parameters – including the numerical values used for the simulations – are summarised in **Supplementary Table 7**.

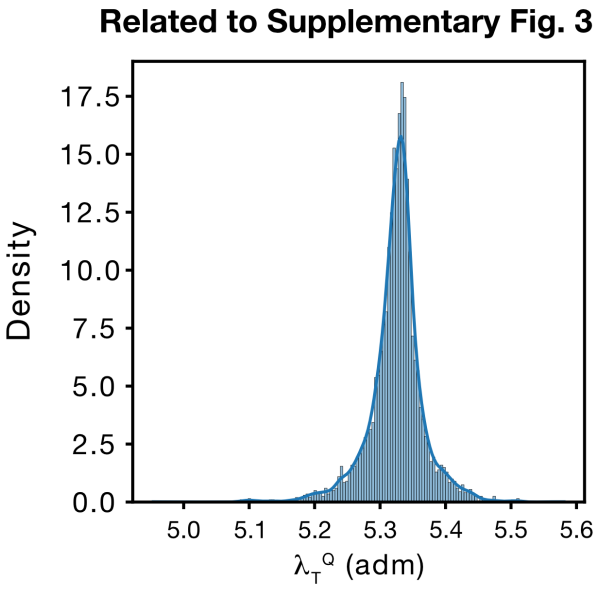

Supplementary Figure 6. Histogram and probability density function for the model parameter λ_T^Q. The distribution of the inferred numerical values for the model parameter λ_T^Q was obtained by repeating the model fitting (**Methods**) 5,000 times (see an instance of the model fitting in **Supplementary Fig. 3**). Mean value calculated from the probability density function: $\overline{\lambda}_T^Q$ = 5.325.

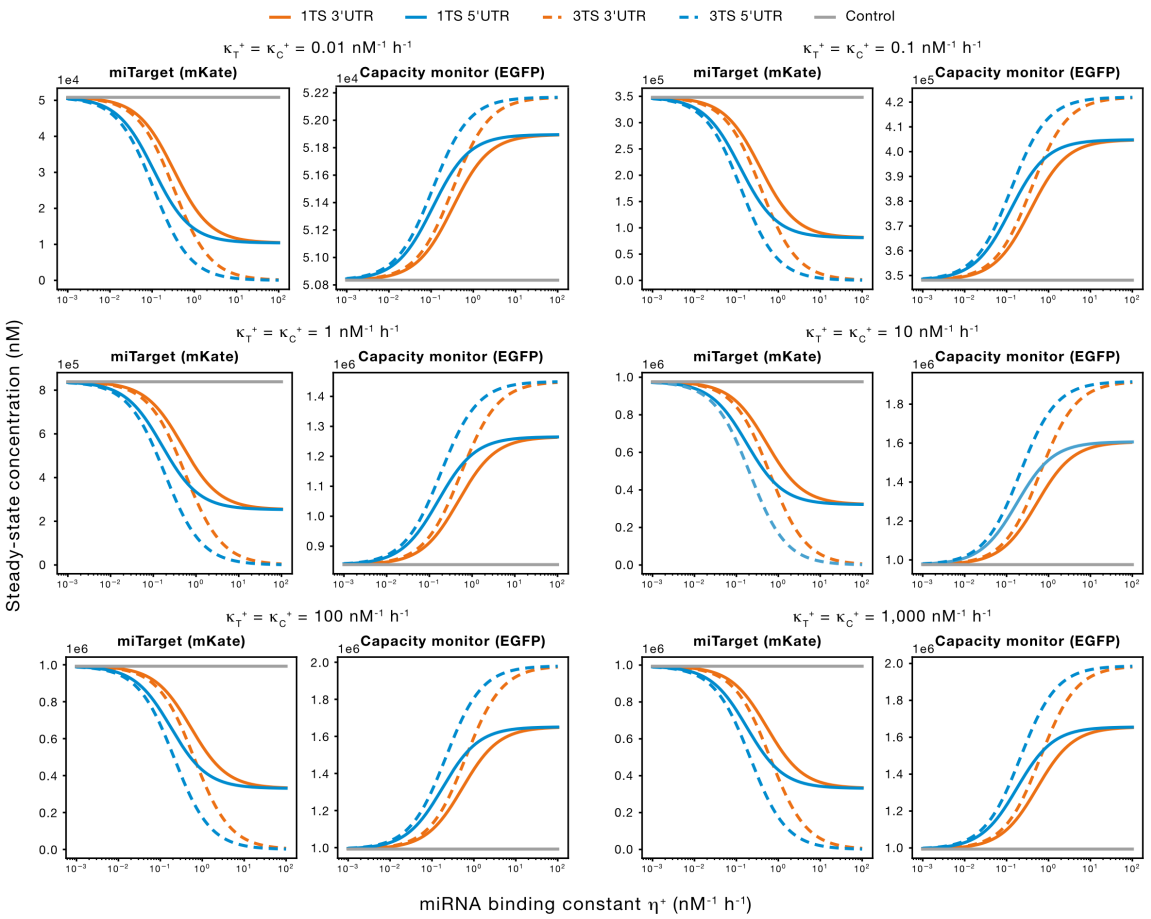

Supplementary Figure 7. The simulated qualitative trend of the protein expression levels does not change when varying κ_T^+ and κ_C^+. The ODE model illustrated in **Fig. 2a** was simulated using different values for the association constants κ_T^+ and κ_C^+ to understand how the miRNA-driven regulation changes the protein expression levels for the *miTarget* (mKate) and the *capacity monitor* (EGFP). The two association constants were set to the same value (i.e., $\kappa_T^+ = \kappa_C^+$) since the two transcripts have similar RNA sequences, hence the binding rate constants κ_T^+ and κ_C^+ may only slightly differ from each other. Numerical simulations show that the qualitative trend of the protein expression levels does not change when varying κ_T^+ and κ_C^+, but the absolute protein levels do. Each colour represents a different design condition that depends on the location and the number of the miRNA target sites at the UTRs of the *miTarget* gene. A description of the model can be found in **Supplementary Notes 1-3**. All the molecular species captured in the model are listed in **Supplementary Table 4**, whilst all the model parameters – including the numerical values used for the simulations – are summarised in **Supplementary Table 5**.

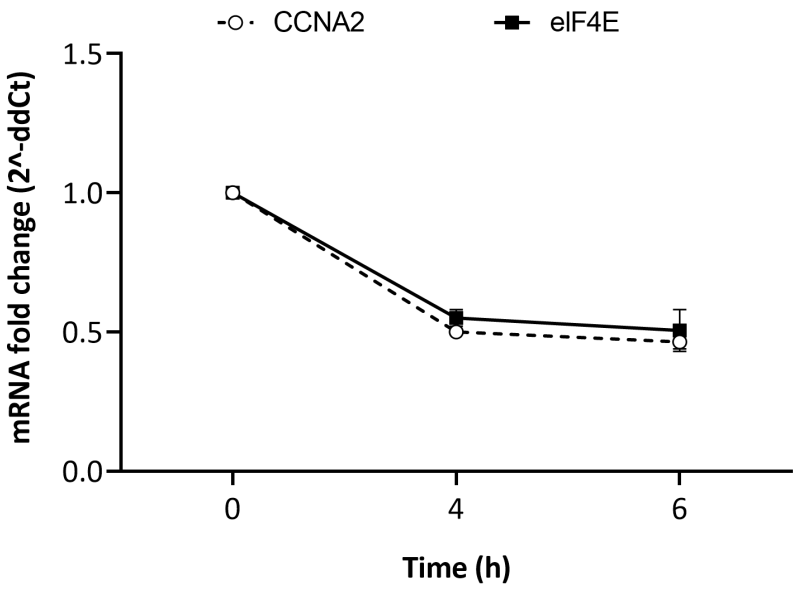

Supplementary Figure 8. CCNA2 and eIF4E half-life in H1299 cells treated with DRB.
mRNA half-life of CCNA2 and eIF4E were measured up to 6 hours post-DRB treatment in wild type cells. All data are plotted as mean +/- SE. SE: standard error. N=2 replicates.

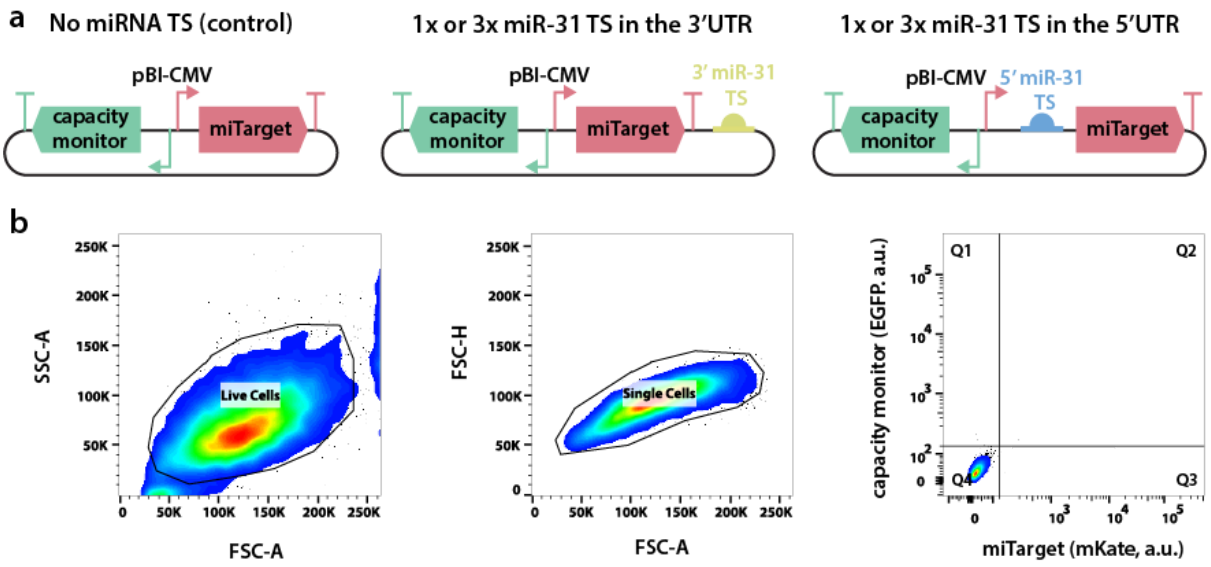

Supplementary Figure 9. Plasmids design and gating strategy for flow cytometry experiments. (a) All plasmids encode for two fluorescent proteins, namely the *capacity monitor* (EGFP) and *miTarget* (mKate) proteins, under the regulation of a bidirectional CMV promoter (pBI-CMV). No miRNA TS (control): plasmid without target sites for miRNA-31. Plasmids encoding for 1x or 3x miR-31 target sites (TS) either in the 3'UTR or 5'UTR of the *miTarget* are used to study the effect of miRNA on resource reallocation. **(b)** Gating strategy, example on non-transfected cells to set the positive threshold for each fluorescence. Left, the recorded events were gated first in the FSC-A vs SSC-A channels to select the Live Cells population. Centre, the Live Cells population was then gated in the FSC-A vs FSC-H channels to select the single-cell population. Right, the geometric mean of cells in the Q2 quadrant (double positive) was pulled out.

Supplementary Table 1. Transfection Tables.

Figure 3c-d

	pBI-F3G	pBI-H1G/H3G/H5G/H7G	pEmpty
Control	2.9 µg		5.6 µg
miR-31 TS		2.9 µg	5.6 µg
Reagent/cells			
Optimem	1450 µL		
Lipofectamine 3000	21.75 µL		
P3000	29 µL		
H1299	3480000		

Figure 4c-d

	pBI-G	pL-A1	pH-3/pH-7	pEmpty
Control	50 ng	50 ng		200 ng
miR-31 TS	50 ng		50 ng	200 ng
Reagent/cells				
Optimem	50 µL			
Lipofectamine 3000	0.75 µL			
P3000	1 µL			
H1299	150000			

Supplementary Table 2. List of plasmids used for this study.

Fig.	Short plasmid name	Full plasmid name	Parts from	GenBank accession code
Fig. 3c-d	pBI-F3G	pBI-CMV1_EGFP_mKate	Clontech 631630	MT891342
Fig. 3c-d	pBI-H1G	pBI-CMV1_EGFP_mKate_1xmiR31TS5'	Clontech 631630	MT891344
Fig. 3c-d	pBI-H3G	pBI-CMV1_EGFP_mKate_3xmiR31TS5'	Clontech 631630	MT891345
Fig. 3c-d	pBI-H5G	pBI-CMV1_EGFP_mKate_1xmiR31TS3'	Clontech 631630	MT891346
Fig. 3c-d	pBI-H7G	pBI-CMV1_EGFP_mKate_3xmiR31TS3'	Clontech 631630	MT891347
Fig. 4c-d	pBI-G	pBI-CMV1_EGFP	Clontech 631630	MT891343
Fig. 4c-d	pL-A1	pT-GTW6-CMV-mKate	(1)	MT891367
Fig. 4c-d	pH-3	pT-GTW6-CMV-mKate_3xmiR31TS5'	(1)	MT891350
Fig. 4c-d	pH-7	pT-GTW6-CMV-mKate_3xmiR31TS3'	(2)	MT891353

Supplementary Table 3. qPCR primers used in this study.

Primer	Function	Sequence (5’-3’)
F7	Forward primer for mKate amplification	GGTGTCTAAGGGCGAAGAGC
F8	Reverse primer for mKate amplification	GCTGGTAGCCAGGATGTCGA
qPCR-EGFP-F	Forward primer for EGFP amplification	AAGGGCATCGACTTCAAG
qPCR-EGFP-R	Reverse primer for EGFP amplification	TGCTTGTCGGCCATGATATG
qPCR-18S-F	Forward primer for 18S amplification	GCTTAATTTGACTCAACACGGGA
qPCR-18S-R	Reverse primer for 18S amplification	AGCTATCAATCTGTCAATCCTGTC
qPCR-GAPDH-F	Forward primer for GAPDH amplification	GAAGATGGTGATGGGATTTC
qPCR-GAPDH-R	Reverse primer for GAPDH amplification	GAAGTTGAAGGTCGGAGT
qPCR-CCNA2-F	Forward primer for CCNA2 amplification	GGGACAAAGCTGGCCTGAATC
qPCR-CCNA2-R	Reverse primer for CCNA2 amplification	AGGTAGGTCTGGTGAAGGTCC
qPCR-eIF4E-F	Forward primer for eIF4E amplification	AGAACAGATGGGCACTCTGX
qPCR-eIF4E-R	Reverse primer for eIF4E amplification	TGAGTAGTCACAGCCAGGC

Supplementary Table 4. Molecular species simulated in the model to study the reallocation of translational resources. Related to Supplementary Notes 1-4.

Description	Species	Units
miTarget mRNA	m_T	nM
Translating *miTarget* mRNA	b_T	nM
miTarget:miRNA mRNA complex	m_T^Q	nM
Translating *miTarget:miRNA* mRNA complex	b_T^Q	nM
miRNA	q	nM
Capacity monitor mRNA	m_C	nM
Translating *capacity monitor* mRNA	b_C	nM
miTarget protein (mKate)	p_T	nM
Capacity monitor protein (EGFP)	p_C	nM
Free ribosomes	r	nM

Supplementary Table 5. Numerical parameters used to simulate the model to study the reallocation of translational resources. Related to Supplementary Notes 1-4.

Description	Parameter	Value	Units
miTarget transcription rate constant	α_T	1	nM h^{-1}
miRNA binding constant	η^+	[0.001, 100]	nM^{-1} h^{-1}
miRNA dissociation constant	η^-	0	h^{-1}
miTarget mRNA degradation rate constant	β_T	0.231	h^{-1}
miTarget:miRNA mRNA degradation rate constant	β_T^Q	1.155	h^{-1}
miTarget translation rate constant	γ_T	53	h^{-1}
miTarget ribosomal scaling factor	n_T	33	Unitless
Association constant between a *miTarget* mRNA and a ribosome	κ_T^+	1	nM^{-1} h^{-1}
Dissociation constant of the *miTarget* translating complex	κ_T^-	0	h^{-1}
miTarget protein degradation rate constant	δ_T	0.027	h^{-1}
miRNA transcription rate constant	α_Q	0.05	nM h^{-1}
miRNA degradation rate constant	β_Q	0.069	h^{-1}
Capacity monitor transcription rate constant	α_C	1	nM h^{-1}
Capacity monitor translation rate constant	γ_C	53	h^{-1}
Capacity monitor ribosomal scaling factor	n_C	33	Unitless
Association constant between a the *Capacity monitor* mRNA and a ribosome	κ_C^+	1	nM^{-1} h^{-1}
Dissociation constant of a *Capacity monitor* translating complex	κ_C^-	0	h^{-1}
Capacity monitor protein degradation rate constant	δ_C	0.027	h^{-1}
Total ribosomes available in the model	r^{Total}	1000	nM

Supplementary Table 6. Molecular species simulated in the model to study the reallocation of degradation resources. Related to Supplementary Note 5.

Description	Species	Units
miTarget mRNA	m_T	nM
Degrading *miTarget:RNase* complex	s_T	nM
miTarget:miRNA mRNA complex	m_T^Q	nM
Degrading *miTarget:miRNA:RNase* complex	s_T^Q	nM
miRNA	q	nM
Endogenous mRNA	m_E	nM
Degrading E*ndogenous:RNase* complex	s_E	nM
Free RNases	g	nM

Supplementary Table 7. Numerical parameters used to simulate the model to study the reallocation of degradation resources. Related to Supplementary Note 5.

Description	Parameter	Value	Units
miTarget transcription rate constant	α_T	1	nM h^{-1}
miRNA binding constant	η^+	{0, 0.5, 1, 2, 4, 8}	nM^{-1} h^{-1}
miRNA dissociation constant	η^-	0	h^{-1}
Association constant between a *miTarget* mRNA and an RNase	β_T^+	1	nM^{-1} h^{-1}
Dissociation constant of a *miTarget:RNase* complex	β_T^-	0	h^{-1}
miTarget:RNase complex degradation rate constant	β_T^{Deg}	1	h^{-1}
Association constant between a *miTarget:miRNA* complex and an RNase	$\beta_{T,Q}^+$	500	nM^{-1} h^{-1}
Dissociation constant of *miTarget:miRNA:RNase* complex	$\beta_{T,Q}^-$	0	h^{-1}
miTarget:miRNA:RNase complex degradation rate constant	$\beta_{T,Q}^{Deg}$	1	h^{-1}
miRNA transcription rate constant	α_Q	0.05	nM h^{-1}
miRNA degradation rate constant	β_Q	0.069	h^{-1}
Endogenous transcription rate constant	α_E	0.1	nM h^{-1}
Association constant between an endogenous mRNA and an RNase	β_E^+	10	nM^{-1} h^{-1}
Dissociation constant of the *Endogenous:RNase* complex	β_E^-	0	h^{-1}
Endogenous:RNase complex degradation rate constant	β_E^{Deg}	1	h^{-1}
Total RNase available in the model	g^{Total}	1	nM
Cell growth rate	μ	0.029	h^{-1}

Supplementary Note 1. Resource-aware model to study reallocation of translational resources.

In what follows we describe the resource-aware deterministic model used to study the reallocation of translational resources (i.e., ribosomes) as introduced in **Fig. 2** and **Fig. 3**. The deterministic model is based on an existing resource-aware modelling framework (2) and considers ribosomes as the main cellular resources shared between co-expressed genes. Our model replaces reaction rates that involve shared translational resources with effective reaction rates that account for the availability of these resources according to the overall demand from co-expressed genes as shown in **Fig. 1b**. The key assumptions underlying the formulation of the model equations are listed and discussed in the main text. Briefly, we make the following assumptions:

1. The shared cellular resource pool for translation (ribosomes) is considered finite and constant.
2. The shared cellular resource pool for RNA degradation (RNases) is considered unlimited.
3. Shared transcriptional resource pools (e.g., RNA polymerases) are not explicitly considered in the model. Such an assumption does not alter the findings of our study as shown in **Supplementary Note 2**.

To derive the deterministic model, we apply the law of mass action to the biochemical reactions shown in **Supplementary Fig. 1**. Hence, we obtain the following set of ordinary differential equations (ODE):

$$\frac{dm_T}{dt} = \alpha_T - \kappa_T^+ \, m_T r + \left(\kappa_T^- + \gamma_T\right) b_T + \eta^- m_T^Q - \left(\beta_T + \eta^+ q\right) m_T$$

$$\frac{db_T}{dt} = \kappa_T^+ \, m_T r - \left(\kappa_T^- + \gamma_T\right) b_T$$

$$\frac{dm_T^Q}{dt} = \eta^+ q \; m_T - \left(\beta_T^Q + \eta^-\right) m_T^Q - \sigma \cdot \kappa_T^+ \, m_T^Q r + \sigma \cdot \left(\kappa_T^- + \gamma_T\right) b_T^Q$$

$$\frac{db_T^Q}{dt} = \kappa_T^+ \, m_T^Q r - \left(\kappa_T^- + \gamma_T\right) b_T^Q \qquad \text{(applies only to the 3' UTR model)}$$

$$\frac{dq}{dt} = \alpha_Q + \left(\beta_T^Q + \eta^-\right) m_T^Q - \left(\beta_Q + \eta^+ \, m_T\right) q$$

$$\frac{dm_C}{dt} = \alpha_C - \beta_C \, m_C - \kappa_C^+ \, m_C r + \left(\kappa_C^- + \gamma_C\right) b_C$$

$$\frac{db_C}{dt} = \kappa_C^+ \, m_C r - \left(\kappa_C^- + \gamma_C\right) b_C$$

$$\frac{dp_T}{dt} = \gamma_T \left(b_T + \sigma \cdot b_T^Q \right) - \delta_T \, p_T$$

$$\frac{dp_C}{dt} = \gamma_C\ b_C - \delta_C\ p_C$$

where the boolean parameter $\sigma \in \{0,\ 1\}$ captures the location of the miR-TS at the UTRs. Specifically, σ is set to 1 if the miR-TS are at the 3' UTR, otherwise σ is set to 0. When considering miR-TS at the 3' UTR (i.e., when $\sigma = 1$), the model captures the additional inhibition of translation by the *miTarget:miRNA* mRNA complex. A list of all the molecular species modelled is reported in **Supplementary Table 4**, whilst a list of all the model parameters – including the numerical values used to simulate the model (see **Supplementary Note 6** for the model parameterisation) – is reported in **Supplementary Table 5**.

Assuming that the translating ribosomal complexes b_T, b_C, and b_T^Q (the latter being considered only in the 3' UTR model) reach their steady state faster than the other molecular species involved in the model, we can make a quasi-steady-state approximation (QSSA) for the dynamics of the translating ribosomal complexes in our proposed resource-aware model. Such an assumption is biologically reasonable since a ribosome typically binds to a transcript with a timescale faster than that associated with the production and degradation of mRNA and protein species. Therefore, assuming a QSSA for the translating ribosomal complexes concentrations, we obtain the following steady-state concentrations – which we denote with a bar:

$$\frac{db_T}{dt} \approx 0 \Rightarrow \bar{b}_T = \frac{\kappa_T^+}{\kappa_T^- + \gamma_T} m_T\, r = \frac{1}{\kappa_T} m_T\, r$$

$$\frac{db_T^Q}{dt} \approx 0 \Rightarrow \bar{b}_T^Q = \frac{\kappa_T^+}{\kappa_T^- + \gamma_T} m_T^Q\, r = \frac{1}{\kappa_T} m_T^Q\, r \qquad \text{(applies only to the in 3' UTR model)}$$

$$\frac{db_C}{dt} \approx 0 \Rightarrow \bar{b}_C = \frac{\kappa_C^+}{\kappa_C^- + \gamma_C} m_C\, r = \frac{1}{\kappa_C} m_C\, r$$

where the lumped parameters κ_T and κ_C denote the effective dissociation constants between the mRNA species and the ribosome species. Substituting these quasi-steady-state concentrations in the resource-aware model yields the reduced ODE model:

$$\frac{dm_T}{dt} = \alpha_T + \eta^-\ m_T^Q - \left(\beta_T + \eta^+\ q\right) m_T$$

$$\frac{dm_T^Q}{dt} = \eta^+\ q\ m_T - \left(\beta_T^Q + \eta^-\right) m_T^Q$$

$$\frac{dq}{dt} = \alpha_Q + \left(\beta_T^Q + \eta^-\right) m_T^Q - \left(\beta_Q + \eta^+\ m_T\right) q$$

$$\frac{dm_C}{dt} = \alpha_C - \beta_C\ m_C$$

$$\frac{dp_T}{dt} = \gamma_T \frac{m_T + \sigma\, m_T^Q}{\kappa_T} r - \delta_T\, p_T$$

$$\frac{dp_C}{dt} = \gamma_C \frac{m_C}{\kappa_C} r - \delta_C\, p_C$$

Assuming a limited constant amount of available translational resources (r^{Total}), we can apply a resource conservation law on the total concentration of translational resources:

$$r^{Total} = r + \overline{b}_T + \overline{b}_T^Q + \overline{b}_C$$

Substituting the steady-state concentrations of the translating ribosomal complexes in the previous equation yields the concentration of free ribosomes:

$$r = \frac{r^{Total}}{1 + \frac{m_T + \sigma\, m_T^Q}{\kappa_T} + \frac{m_C}{\kappa_C}}$$

Substituting the concentration of free ribosomes in the reduced model yields the resource-aware ODE model (**Fig. 2a**):

$$\frac{dm_T}{dt} = \alpha_T + \eta^- m_T^Q - \left(\beta_T + \eta^+ q\right) m_T$$

$$\frac{dm_T^Q}{dt} = \eta^+ q\; m_T - \left(\beta_T^Q + \eta^-\right) m_T^Q$$

$$\frac{dq}{dt} = \alpha_Q + \left(\beta_T^Q + \eta^-\right) m_T^Q - \left(\beta_Q + \eta^+\, m_T\right) q$$

$$\frac{dm_C}{dt} = \alpha_C - \beta_C\, m_C$$

$$\frac{dp_T}{dt} = \gamma_T^{Eff} + \gamma_{T,Q}^{Eff} - \delta_T\, p_T$$

$$\frac{dp_C}{dt} = \gamma_C^{Eff} - \delta_C\, p_C$$

where the effective translation rate constants are defined as:

$$\gamma_T^{Eff} = \gamma_T \cdot \frac{\frac{m_T}{\kappa_T}}{1 + \frac{m_T + \sigma\, m_T^Q}{\kappa_T} + \frac{m_C}{\kappa_C}} \cdot r^{Total} = \gamma_T \cdot \frac{\frac{m_T}{\kappa_T}}{1 + \frac{m_C}{\kappa_C} + \frac{\sigma\, m_T^Q}{\kappa_T} + \frac{m_T}{\kappa_T}} \cdot\; r^{Total} = \gamma_T \cdot f_T\left(m_T,\, \sigma\, m_T^Q,\, m_C\right) \cdot r^{Total}$$

$$\gamma_{T,Q}^{Eff} = \gamma_T \cdot \frac{\frac{\sigma\, m_T^Q}{\kappa_T}}{1+\frac{m_T+\sigma\, m_T^Q}{\kappa_T}+\frac{m_C}{\kappa_C}} \cdot r^{Total} = \gamma_T \cdot \frac{\frac{\sigma\, m_T^Q}{\kappa_T}}{1+\frac{m_C}{\kappa_C}+\frac{m_T}{\kappa_T}+\frac{\sigma\, m_T^Q}{\kappa_T}} \cdot r^{Total} = \gamma_T \cdot f_{T,Q}\left(m_T,\ \sigma\ m_T^Q,\ m_C\right) \cdot r^{Total}$$

$$\gamma_C^{Eff} = \gamma_C \cdot \frac{\frac{m_C}{\kappa_C}}{1+\frac{m_T+\sigma\, m_T^Q}{\kappa_T}+\frac{m_C}{\kappa_C}} \cdot r^{Total} = \gamma_C \cdot \frac{\frac{m_C}{\kappa_C}}{1+\frac{m_T+\sigma\, m_T^Q}{\kappa_T}+\frac{m_C}{\kappa_C}} \cdot r^{Total} = \gamma_T \cdot f_C\left(m_T,\ \sigma\ m_T^Q,\ m_C\right) \cdot r^{Total}$$

These lumped parameters represent the core of the resource-aware model and reflect the dependency of the mRNA translation rates on the effective availability of translational resources in the cell. This dependency is captured via the regulatory functions f_T, $f_{T,Q}$, and f_C. The use of effective rates that take into account availability of shared cellular resources is conceptually illustrated in **Fig. 1b**.

The parameters used to simulate the model are summarised in **Supplementary Table 5**.

Supplementary Note 2. Negligible effects of transcriptional burden in the study of post-transcriptional resources reallocation.

As we are focusing on post-transcriptional events, the model does not explicitly consider shared pools of transcriptional resources (**Supplementary Note 1**). The inclusion or not of a shared transcriptional resource pool does not affect the results and the conclusions since variations in transcriptional burden can be accounted for by a change in the transcription rate constants α_T, α_C, and α_Q.

Similarly to the derivation done in **Supplementary Note 1** for the resource-aware translation dynamics, we can augment the model to also consider a limited pool of shared transcriptional resources (e.g., RNA polymerases) and thus capture transcriptional burden via effective transcription rate constants. Let a_T, a_C, and a_Q be the DNA concentrations for the *miTarget* gene, the *Capacity monitor* gene, and the *miRNA*; respectively. Let h^{Total} and h denote the available amounts of total and free transcriptional resources, respectively. Then, the ODEs associated with the RNA species can be rewritten using the effective transcription rate constants α_T^{Eff} (*miTarget*), α_C^{Eff} (*Capacity monitor*), and α_Q^{Eff} (*miRNA*) as follows:

$$\frac{dm_T}{dt} = \alpha_T^{Eff} + \eta^- m_T^Q - \left(\beta_T + \eta^+ q\right) m_T$$

$$\frac{dm_T^Q}{dt} = \eta^+ q\ m_T - \left(\beta_T^Q + \eta^-\right) m_T^Q$$

$$\frac{dq}{dt} = \alpha_Q^{Eff} + \left(\beta_T^Q + \eta^-\right) m_T^Q - \left(\beta_Q + \eta^+\ m_T\right) q$$

$$\frac{dm_C}{dt} = \alpha_C^{Eff} - \beta_C\ m_C$$

where the effective transcription rate constants are defined as:

$$\alpha_T^{Eff} = \alpha_T \cdot \frac{\frac{a_T}{\nu_T}}{1+\frac{a_T}{\nu_T}+\frac{a_C}{\nu_C}+\frac{a_Q}{\nu_Q}} \cdot h^{Total} = \alpha_T \cdot f_T^H\left(a_T, a_C, a_Q\right) \cdot h^{Total}$$

$$\alpha_Q^{Eff} = \alpha_Q \cdot \frac{\frac{a_Q}{\nu_Q}}{1+\frac{a_T}{\nu_T}+\frac{a_C}{\nu_C}+\frac{a_Q}{\nu_Q}} \cdot h^{Total} = \alpha_Q \cdot f_Q^H\left(a_T, a_C, a_Q\right) \cdot h^{Total}$$

$$\alpha_C^{Eff} = \alpha_C \cdot \frac{\frac{a_C}{\nu_C}}{1+\frac{a_T}{\nu_T}+\frac{a_C}{\nu_C}+\frac{a_Q}{\nu_Q}} \cdot h^{Total} = \alpha_C \cdot f_C^H\left(a_T, a_C, a_Q\right) \cdot h^{Total}$$

and ν_T, ν_C, and ν_Q are the effective dissociation constants between a DNA strand and an RNA polymerase for the *miTarget* gene, the *Capacity monitor* gene, and the *miRNA*; respectively. These

lumped parameters α_T^{Eff}, α_C^{Eff}, and α_Q^{Eff} exclusively depend on the DNA concentrations (a_T, a_C, and a_Q). Therefore, the transcriptional burden may alter the transcriptional profiles of the mRNAs. Nevertheless, the miRNA-driven regulation doesn't affect the effective transcriptional rate constants, neither implicitly nor explicitly. Hence, the effective transcription rates can be considered constant within the scope of this study. Without loss of generality, the superscript "Eff" associated with the effective transcription rate constants is omitted to simplify notations throughout the study.

Supplementary Note 3. Embedding polysomes into the resource-aware model to study reallocation of translational resources.

The model derived in **Supplementary Note 1** considers a set of 1:1 stoichiometric reactions between a transcript and a ribosome. However, a single transcript can be simultaneously translated by a group of ribosomes forming a complex known as polysome. Similarly to what was done in a previous resource-aware framework (3), the model can implicitly account for this by rescaling a subset of the model parameters according to the ribosome footprint on a transcript (4, 5).
The key idea consists of considering a series of mRNA spots in lieu of a single mRNA spot per transcript. More specifically, to account for polysomes, the model considers for each transcript a fixed number of mRNA spots that depends on the ribosome footprint size. Hence, each ribosome can bind only to a single mRNA spot. To capture this behaviour, the mRNA transcript concentrations are artificially augmented by rescaling a subset of model parameters as follows:

$$\alpha_T' = n_T\,\alpha_T$$

$$\alpha_Q' = n_T\,\alpha_Q$$

$$\alpha_C' = n_C\,\alpha_C$$

$$\eta^{+\prime} = \frac{\eta^+}{n_T}$$

where n_T and n_C are the maximum ribosomal densities – as defined in **Supplementary note 4** – achievable for the *miTarget* and the *capacity monitor*, respectively. Without loss of generality, we omit the prime symbol in the previous parameters to simplify the notation. Although the miRNA does not undergo a translation process (by definition), the miRNA transcription rate constant needs to be rescaled in order to maintain consistency between the miRNA concentration and the *miTarget* mRNA spots (i.e., a 1:1 stoichiometric ratio).
Under the previous considerations, the corresponding ODE model becomes:

$$\frac{dm_T}{dt} = n_T\,\alpha_T + \eta^-\,m_T^Q - \left(\beta_T + \frac{\eta^+}{n_T}\,q\right) m_T$$

$$\frac{dm_T^Q}{dt} = \frac{\eta^+}{n_T}\,q\;\; m_T - \left(\beta_T^Q + \eta^-\right) m_T^Q$$

$$\frac{dq}{dt} = n_T\,\alpha_Q + \left(\beta_T^Q + \eta^-\right) m_T^Q - \left(\beta_Q + \frac{\eta^+}{n_T}\;\; m_T\right) q$$

$$\frac{dm_C}{dt} = n_C\,\alpha_C - \beta_C\;\, m_C$$

$$\frac{dp_T}{dt} = \gamma_T^{Eff} - \delta_T\;\, p_T$$

$$\frac{dp_C}{dt} = \gamma_C^{Eff} - \delta_C \, p_C$$

The numerical values for the rescaling factors n_T and n_C are reported in **Supplementary Table 5**. To calculate their values, a general ribosome footprint size of ~30 nt (4, 5), which is equivalent to ~10 amino acids, is considered. Since the two genes have the same transcript length of ~1 kbp (see the model parameter values provided in **Supplementary Note 6**), then the rescaling factors can be calculated as:

$$n_T = n_C = \frac{1\ kbp}{30\ bp} \simeq 33$$

which corresponds to the maximum number of translating ribosomes allowed to simultaneously translate a single mRNA transcript.

Supplementary Note 4. Analytical steady-state solution of the resource-aware model.

The RNA dynamics can be approximated to a quasi-steady state in order to obtain an analytical steady-state solution of the model presented in **Supplementary Note 1**. Therefore, assuming that the RNA concentrations m_T, m_T^Q, q, and m_C reach their steady state faster than the protein concentrations p_T and p_C, we can make a QSSA for the RNA dynamics in the reduced model described in **Supplementary Note 1**. Such an assumption is biologically reasonable since RNA species are typically produced and degraded faster than protein species. Assuming a quasi-steady-state approximation of the RNA dynamics in the reduced ODE model (**Supplementary Note 1**), we obtain the following algebraic system of equations:

$$\frac{dm_T}{dt} \approx 0 \Rightarrow n_T \alpha_T + \eta^- \overline{m}_T^Q - \left(\beta_T + \frac{\eta^+}{n_T} \overline{q}\right) \overline{m}_T = 0$$

$$\frac{dm_T^Q}{dt} \approx 0 \Rightarrow \frac{\eta^+}{n_T} \overline{q}\, \overline{m}_T - \left(\beta_T^Q + \eta^-\right) \overline{m}_T^Q = 0$$

$$\frac{dq}{dt} \approx 0 \Rightarrow n_T \alpha_Q + \left(\beta_T^Q + \eta^-\right) \overline{m}_T^Q - \left(\beta_Q + \frac{\eta^+}{n_T}\, \overline{m}_T\right) \overline{q} = 0$$

$$\frac{dm_C}{dt} \approx 0 \Rightarrow n_C \alpha_C - \beta_C\, \overline{m}_C = 0$$

Solving this algebraic system of equations yields the following QSSA for the RNA dynamics:

$$\overline{m}_T = \frac{n_T \alpha_T}{\beta_T + \frac{\alpha_Q \eta^+ \beta_T^Q}{\beta_Q \left(\beta_T^Q + \eta^-\right)}}$$

$$\overline{m}_T^Q = \frac{n_T \alpha_T}{\beta_T^Q + \frac{\beta_T \beta_Q \left(\beta_T^Q + \eta^-\right)}{\alpha_Q \eta^+}}$$

$$\overline{q} = \frac{n_T \alpha_T}{\beta_Q}$$

$$\overline{m}_C = \frac{n_C \alpha_C}{\beta_C}$$

We then define the resource demand coefficients for the *miTarget* (ρ_T and ρ_T^Q) and *capacity monitor* (ρ_C) as:

$$\rho_T = \frac{\overline{m}_T}{\kappa_T} = \frac{n_T \alpha_T}{\kappa_T \left(\beta_T + \frac{\alpha_Q \eta^+ \beta_T^Q}{\beta_Q \left(\beta_T^Q + \eta^-\right)}\right)}$$

$$\rho_T^Q = \frac{\overline{m}_T^Q}{\kappa_T} = \frac{n_T \alpha_T}{\kappa_T \left(\beta_T^Q + \frac{\beta_T \beta_Q \left(\beta_T^Q + \eta^-\right)}{\alpha_Q \eta^+}\right)}$$

$$\rho_C = \frac{\overline{m}_C}{\kappa_C} = \frac{n_C \alpha_C}{\kappa_C \beta_C}$$

Hence, we can rewrite the effective translation rate constants (**Supplementary Note 1**) as:

$$\gamma_T^{Eff} = \gamma_T \cdot \frac{\rho_T}{1+\rho_C+\rho_T+\sigma \rho_T^Q} \cdot r^{Total}$$

$$\gamma_{T,Q}^{Eff} = \gamma_T \cdot \frac{\sigma \rho_T^Q}{1+\rho_C+\rho_T+\sigma \rho_T^Q} \cdot r^{Total}$$

$$\gamma_C^{Eff} = \gamma_C \cdot \frac{\rho_C}{1+\rho_T+\sigma \rho_T^Q+\rho_C} \cdot r^{Total}$$

Finally, we solve for the steady-state protein concentrations of both the *miTarget* and the *capacity monitor* by setting their ODE to zero:

$$\frac{dp_T}{dt} \approx 0 \Rightarrow \gamma_T^{Eff} + \gamma_{T,Q}^{Eff} - \delta_T \overline{p}_T = 0 \Rightarrow \overline{p}_T = \frac{\gamma_T^{Eff}+\gamma_{T,Q}^{Eff}}{\delta_T}$$

$$\frac{dp_C}{dt} \approx 0 \Rightarrow \gamma_C^{Eff} - \delta_C \overline{p}_C = 0 \Rightarrow \overline{p}_C = \frac{\gamma_C^{Eff}}{\delta_C}$$

Substituting the effective translation rate constants into the previous steady-state values, we obtain the following analytical steady-state solution for the protein concentrations:

$$\overline{p}_T = \frac{\gamma_T}{\delta_T} \cdot \frac{\rho_T+\sigma \rho_T^Q}{1+\rho_C+\rho_T+\sigma \rho_T^Q} \cdot r^{Total}$$

$$\overline{p}_C = \frac{\gamma_C}{\delta_C} \cdot \frac{\rho_C}{1+\rho_T+\sigma \rho_T^Q+\rho_C} \cdot r^{Total}$$

We note that the analytical steady-state solutions for the protein concentration of both genes depend on the three resource demand coefficients ρ_T, ρ_T^Q, and ρ_C.

Similarly, we can derive an analytical expression for the concentration of free ribosome at steady state:

$$\overline{r} = \frac{r^{Total}}{1+\rho_T+\sigma \rho_T^Q+\rho_C}$$

We note that the previous steady-state expression resembles a repressing Hill regulatory function that depends on the resource demand coefficients.

Finally, we can derive an analytical expression for the steady-state ribosomal densities for the *miTarget* (RD_T) and the *capacity monitor* (RD_C). Here, we define the ribosomal density as the number of translating ribosomes per transcript. Therefore, the ribosomal density for the *miTarget* gene at steady state can be calculated as:

$$RD_T = \frac{\bar{b}_T^{Tot}}{\bar{m}_T^{Tot} + \bar{b}_T^{Tot}} = \frac{\bar{b}_T + \bar{b}_T^Q}{\bar{m}_T + \bar{m}_T^Q + \bar{b}_T + \bar{b}_T^Q} = \frac{\frac{\rho_T + \sigma\,\rho_T^Q}{1+\rho_C+\rho_T+\sigma\,\rho_T^Q} \cdot r^{Total}}{\kappa_T\left(\rho_T + \sigma\,\rho_T^Q\right) + \frac{\rho_T+\sigma\,\rho_T^Q}{1+\rho_C+\rho_T+\sigma\,\rho_T^Q} \cdot r^{Total}} = \frac{\frac{r^{Total}}{1+\rho_T+\sigma\,\rho_T^Q+\rho_C}}{\kappa_T + \frac{r^{Total}}{1+\rho_T+\sigma\,\rho_T^Q+\rho_C}} = \frac{\bar{r}}{\kappa_T + \bar{r}}$$

Similarly the steady-state ribosomal density for the *capacity monitor* gene is given as:

$$RD_C = \frac{\bar{b}_C}{\bar{m}_C + \bar{b}_C} = \frac{\frac{\rho_C}{1+\rho_T+\sigma\,\rho_T^Q+\rho_C} \cdot r^{Total}}{\kappa_T\,\rho_C + \frac{\rho_C}{1+\rho_T+\sigma\,\rho_T^Q+\rho_C} \cdot r^{Total}} = \frac{\frac{r^{Total}}{1+\rho_T+\sigma\,\rho_T^Q+\rho_C}}{\kappa_C + \frac{r^{Total}}{1+\rho_T+\sigma\,\rho_T^Q+\rho_C}} = \frac{\bar{r}}{\kappa_C + \bar{r}}$$

Looking at these analytical expressions, we observe that the ribosomal densities depend on the steady-state concentration of free ribosomes via an activating Hill function. Although the analytical expressions for RD_T and RD_C look similar, they differ in terms of the half-saturation constants (κ_T and κ_C, respectively). These half-saturation constants correspond to the effective dissociation constant between the ribosome and the respective transcripts.

Supplementary Note 5. Resource-aware model to study reallocation of RNA degradation resources.

Here we describe the resource-aware deterministic model used to study the reallocation of RNA degradation resources (i.e., RNases) in **Fig. 4**. The deterministic model extends the ODE model described in **Supplementary Note 1** and considers both protein translation and RNA degradation. Once again, our model replaces reaction rates that involve shared cellular resources (in this case ribosomes and RNases) with effective reaction rates that account for the availability of these resources according to the overall demand from competing genes as shown in **Fig. 1b**. The key assumptions underlying the formulation of the model equations are as stated for the model in **Supplementary Note 1** except for *Assumption 2*, as we here assume that the shared cellular resource pool for RNA degradation is finite and constant. Briefly, we recap the assumptions in the following list:

1. The shared cellular resource pool for translation (ribosomes) is considered finite and constant.
2. The shared cellular resource pool for RNA degradation (RNases) is considered finite and constant.
3. Shared transcriptional resource pools (e.g., RNA polymerases) are not explicitly considered in the model. Such an assumption does not alter the findings of our study as shown in **Supplementary Note 2**.

To derive the deterministic model, we apply the law of mass action to the biochemical reactions shown in **Supplementary Fig. 2**. Here, we omit all biochemical reactions associated with mRNA translation (**Supplementary Fig. 1**). This is motivated by the fact that we use this model to study mRNA degradation and not protein production. Therefore, as demonstrated in **Supplementary Note 1**, the ODEs describing the RNA dynamics do not embed any term related to RNA translation if the QSSA of translating ribosomal complexes holds true. Hence, we obtain the following set of ODE:

$$\frac{dm_T}{dt} = \alpha_T + \eta^- m_T^Q + \beta_T^- s_T - \left(\beta_T^+ g + \eta^+ q + \mu\right) m_T$$

$$\frac{ds_T}{dt} = \beta_T^+ m_T g - \left(\beta_T^- + \beta_T^{Deg} + \mu\right) s_T$$

$$\frac{dm_T^Q}{dt} = \eta^+ q m_T + \beta_{T,Q}^- s_T^Q - \left(\beta_{T,Q}^+ g + \eta^- + \mu\right) m_T^Q$$

$$\frac{ds_T^Q}{dt} = \beta_{T,Q}^+ m_T^Q g - \left(\beta_{T,Q}^- + \beta_{T,Q}^{Deg} + \mu\right) s_T^Q$$

$$\frac{dq}{dt} = \alpha_Q + \beta_{T,Q}^{Deg} d_T^Q + \eta^- m_T^Q - \left(\beta_Q + \eta^+ m_T\right) q$$

$$\frac{dm_C}{dt} = \alpha_C + \beta_C^- s_C - \left(\beta_C^+ g + \mu\right) m_C$$

$$\frac{ds_C}{dt} = \beta_C^+ \, m_C \, g \, - \left(\beta_C^- + \beta_C^{Deg} + \, \mu\right) s_C$$

In contrast to the model described in **Supplementary Note 1**, the location of the miR-TS at the UTRs does not change the model behaviour (i.e., no boolean parameter σ is used here). All molecular species modelled here – including their description – are summarised in **Supplementary Table 6**, whilst all the model parameters – including the numerical values used to simulate the model (see **Supplementary Note 6** for the model parameterisation) – are listed in **Supplementary Table 7**.
In contrast to the translating ribosomal complexes described in **Supplementary Note 1**, the degrading *mRNA:RNase* complexes s_T, s_C, and s_T^Q do not reach their steady-state values faster than the other molecular species involved in the model. Hence, we cannot make a QSSA for the dynamics of the degrading *mRNA:RNase* complexes.
Assuming a limited amount of available degradation resources (g^{Total}), we can apply a resource conservation law on the total available amount of degradation resources:

$$g^{Total} = g \, + s_T + s_T^Q + s_C$$

which yields the concentration of free RNases:

$$g = g^{Total} - s_T + s_T^Q + s_C$$

Substituting the concentration of free RNases in the previous ODEs yields the resource-aware ODE model (**Fig. 4a**):

$$\frac{dm_T}{dt} = \alpha_T + \eta^- \, m_T^Q + \beta_T^- \, s_T - \left(\beta_T^{Eff} + \eta^+ \, q\right) m_T$$

$$\frac{ds_T}{dt} = \beta_T^+ \, m_T \, g \, - \left(\beta_T^- + \beta_T^{Deg} + \, \mu\right) s_T$$

$$\frac{dm_T^Q}{dt} = \eta^+ \, q \, \, m_T + \beta_{T,Q}^- \, s_T^Q - \left(\beta_{T,Q}^{Eff} + \eta^-\right) m_T^Q$$

$$\frac{ds_T^Q}{dt} = \beta_{T,Q}^+ \, m_T^Q \, g \, - \left(\beta_{T,Q}^- + \beta_{T,Q}^{Deg} + \, \mu\right) s_T^Q$$

$$\frac{dq}{dt} = \alpha_Q + \beta_{T,Q}^{Deg} \, d_T^Q + \eta^- \, m_T^Q - \left(\beta_Q + \eta^+ \, m_T\right) q$$

$$\frac{dm_C}{dt} = \alpha_C + \beta_C^- \, s_C - \beta_C^{Eff} \, m_C$$

$$\frac{ds_C}{dt} = \beta_C^+ \, m_C \, g \, - \left(\beta_C^- + \beta_C^{Deg} + \, \mu\right) s_C$$

where the effective degradation rate constants are defined as:

$$\beta_T^{Eff} = \beta_T^+ g + \mu = \beta_T^+ \left(g^{Total} - s_T + s_T^Q + s_C \right) + \mu$$

$$\beta_{T,Q}^{Eff} = \beta_{T,Q}^+ g + \mu = \beta_{T,Q}^+ \left(g^{Total} - s_T + s_T^Q + s_C \right) + \mu$$

$$\beta_C^{Eff} = \beta_C^+ g + \mu = \beta_C^+ \left(g^{Total} - s_T + s_T^Q + s_C \right) + \mu$$

These lumped parameters represent the core of the resource-aware model to study RNA degradation and reflect the dependency of the mRNA degradation rates on the effective availability of RNA degradation resources in the cell. Note that these lumped parameters do not depend on the location of the miR-TS at the UTRs. This explains why the location of the target sites at the UTRs does not alter the mRNA degradation profiles of either the *miTarget* or the *capacity monitor* genes.
The parameters used to simulate the model are summarised in **Supplementary Table 7**.

Supplementary Note 6. Model parameterisation.

To qualitatively simulate the different instances of the ODE model described in **Supplementary Notes 1-5**, we select a set of characteristic values so that the simulated dynamical behaviours are coherent with the experimental design of the two-gene circuit used in this study. More specifically, the two genes encode a DNA sequence to produce two different fluorescent proteins:

1. An mKate protein (red fluorescent protein) which represents the *miTarget* – or the miRNA sensor – in the circuit illustrated in **Fig. 1**.
2. An EGFP (enhanced green fluorescent protein) which represents the *Capacity monitor* in the circuit illustrated in **Fig. 1**.

The model parameters used to simulate the model in **Fig. 2** and **Fig. 3** of the main text are listed in **Supplementary Table 5**. To derive characteristic values for the transcription rate constants associated with these two exogenous genes, we first need to understand what could be the transcription rate constant associated with an endogenous gene. We consider an mRNA transcription rate of ~2.4 kbp/min (BNID: 111156, https://bionumbers.hms.harvard.edu/), which is equivalent to ~144 kbp/h, and an endogenous transcript length of ~1300 bp (CCNA2 gene; Gene ID: 890, https://www.ncbi.nlm.nih.gov/gene/890). Hence, the endogenous gene is transcribed at a rate of ~110 transcripts per hour. We assume an endogenous DNA concentration for the endogenous DNA sequence of ~0.001 nM (BNID: 108456, https://bionumbers.hms.harvard.edu/), hence the endogenous transcription rate constant is equivalent to ~0.1 nM/h. Keeping the transcription rate constant for the endogenous gene, we can then proceed to calculate the transcription rate constants for the exogenous genes. We assume that the transcription rate constants associated with the two exogenous genes differ from the one associated with the endogenous gene by an order of magnitude, therefore we set their values to ~1 nM/h. To set the transcription rate constant for the *miRNA*, we assume that the *miRNA* is transcribed at a rate of ~55 transcripts per hour, which is half of the value associated with the endogenous gene. This value is motivated by the fact that an endogenous miRNA may be encoded in an intron, hence the DNA sequence that needs to be transcribed can be longer than the miRNA itself. Also, a transcribed miRNA undergoes a maturation process that can further delay the miRNA biogenesis. Assuming an endogenous DNA concentration for the endogenous DNA sequence carrying the *miRNA* of ~0.001 nM (BNID: 108456, https://bionumbers.hms.harvard.edu/), the transcription rate constant for the *miRNA* is equivalent to ~0.05 nM/h. To set the translation rate constants, we consider a ribosome translocation rate of ~3.5 codons/s (6), which is equivalent to 12,600 codons/h, and a length of 238 amino acids for the *capacity monitor* (EGFP) and the *miTarget* (mKate). To set the RNA degradation rate constants, we consider a half-life for the *miTarget* and *capacity monitor* of ~3 hours (7), and a half-life for the *miRNA* of ~10 hours (8). The *miTarget:miRNA* mRNA degradation rate constant β_T^Q is assumed to be five-fold ($\lambda_T^Q \simeq 5$) larger than the *miTarget* mRNA degradation rate constant β_T. This characteristic value is inferred from the distribution of the parameter λ_T^Q obtained by repeating the model fitting 5,000 times (see **Supplementary Fig. 3**) and shown in **Supplementary Fig. 6** (mean value: λ_T^Q = 5.325). To set the protein degradation rate constants, we consider a half-life for the *miTarget* and *capacity monitor* of ~26 hours (9). RNA and protein degradation rate constants incorporate the cell

dilution rate into their values. The miRNA binding constant η^+ is considered as an independent variable and thus is not set to a fixed value but rather spans a range of reasonable characteristic values. To set the association constants between a transcript and a ribosome, we simulate the ODE model with different values for the association constants κ_T^+ and κ_C^+ to understand how the miRNA-driven regulation changes the protein expression levels for the *miTarget* and the *capacity monitor* (**Supplementary Fig. 7**). To simplify the model, we assume that the two association constants are set to the same value, that is $\kappa_T^+ = \kappa_C^+$. This is motivated by the fact that the two transcripts have similar RNA sequences, hence the binding rate constants κ_T^+ and κ_C^+ may only slightly differ from each other. Numerical simulations show that the qualitative trend of the protein expression levels does not change when varying κ_T^+ and κ_C^+, but the absolute protein levels do as shown in **Supplementary Fig. 7**. Nevertheless, as we are interested in studying the qualitative trend for the protein expression levels upon miRNA action, we assume that the association constants κ_T^+ and κ_C^+ are set to a characteristic value that guarantees coherent protein expression levels comparable to those observed experimentally in **Fig. 2b**. To simplify the model, we assume that all the dissociation constants associated with the unbinding reactions (η^-, κ_T^-, and κ_C^-) are set to zero. We argue that such a choice does not affect the predictive power of the model since these dissociation constants are combined with other parameters throughout the model – more specifically, β_T^Q (i.e., $\beta_T^Q + \eta^-$), γ_T (i.e., $\gamma_T + \kappa_T^-$), and γ_C (i.e., $\gamma_C + \kappa_C^-$); respectively. Intuitively, the unbinding reactions cannot be predominant over the mRNA degradation (i.e., $\beta_T^Q + \eta^- \gg \eta^-$) and translation processes (i.e., $\gamma_T + \kappa_T^- \gg \kappa_T^-$, and $\gamma_C + \kappa_C^- \gg \kappa_C^-$), so their characteristic values can be embedded (and so neglected) into the mRNA degradation and translation rate constants without loss of generality. The total amount of translational resources available in the model is set to a characteristic value of 1,000 nM as reported in a previous study (10).

The model parameters used to simulate the model in **Fig. 4** are listed in **Supplementary Table 7**. Unless otherwise specified, all the model parameters have the same characteristic values as given for the model instance simulated in **Fig. 2** and **Fig.3**. To set the cell growth rate constant (equivalent to the dilution rate constant), we consider a cell division rate of ~24 hours (BNID: 106813, https://bionumbers.hms.harvard.edu/). The endogenous mRNA transcription rate is set to 0.1 nM/h, which accounts for the smaller concentration of an endogenous gene (i.e., ~0.001 nM; BNID: 108456, https://bionumbers.hms.harvard.edu/). To set the parameters associated with the mRNA degradation dynamics (β_T^+, β_T^{Deg}, $\beta_{T,Q}^+$, $\beta_{T,Q}^{Deg}$, β_E^+, β_E^{Deg}, and g^{Total}), we conduct an empirical search on the model parameters so as to obtain a simulated dynamical behaviour coherent with the mRNA degradation dynamics of an endogenous gene similar to the ones considered in this study (CCNA2 and eIF4E). Similarly to the previous case, we assume that all the dissociation constants associated with the unbinding reactions (η^-, β_T^-, and β_E^-) are set to zero. The miRNA binding constant η^+ is still considered as an independent variable, which takes values from a discrete set of reasonable values aimed to study the reallocation of RNA degrading resources.

References

1. Cella,F., Wroblewska,L., Weiss,R. and Siciliano,V. (2018) Engineering protein-protein devices for multilayered regulation of mRNA translation using orthogonal proteases in mammalian cells. *Nature Communications*, **9**.

2. Frei,T., Cella,F., Tedeschi,F., Gutiérrez,J., Stan,G.-B., Khammash,M. and Siciliano,V. (2020) Characterization and mitigation of gene expression burden in mammalian cells. *Nat. Commun.*, **11**, 4641.

3. Qian,Y., Huang,H.-H., Jiménez,J.I. and Del Vecchio,D. (2017) Resource Competition Shapes the Response of Genetic Circuits. *ACS Synth. Biol.*, **6**, 1263–1272.

4. Ingolia,N.T., Ghaemmaghami,S., Newman,J.R.S. and Weissman,J.S. (2009) Genome-wide analysis in vivo of translation with nucleotide resolution using ribosome profiling. *Science*, **324**, 218–223.

5. Gobet,C. and Naef,F. (2017) Ribosome profiling and dynamic regulation of translation in mammals. *Curr. Opin. Genet. Dev.*, **43**, 120–127.

6. Yan,X., Hoek,T.A., Vale,R.D. and Tanenbaum,M.E. (2016) Dynamics of Translation of Single mRNA Molecules In Vivo. *Cell*, **165**, 976–989.

7. He,L., Binari,R., Huang,J., Falo-Sanjuan,J. and Perrimon,N. (2019) In vivo study of gene expression with an enhanced dual-color fluorescent transcriptional timer. *Elife*, **8**.

8. Zlotorynski,E. (2019) Insights into the kinetics of microRNA biogenesis and turnover. *Nat. Rev. Mol. Cell Biol.*, **20**, 511.

9. Nash,K.L. and Lever,A.M.L. (2004) Green fluorescent protein: green cells do not always indicate gene expression. *Gene Ther.*, **11**, 882–883.

10. Jones,R.D., Qian,Y., Siciliano,V., DiAndreth,B., Huh,J., Weiss,R. and Del Vecchio,D. (2020) An endoribonuclease-based feedforward controller for decoupling resource-limited genetic modules in mammalian cells. *Nat. Commun.*, **11**, 5690.